



**CHALMERS**  
UNIVERSITY OF TECHNOLOGY

## **Generalized Langevin dynamics in multiphase direct numerical simulations using hydrodynamically optimized memory kernels**

Downloaded from: <https://research.chalmers.se>, 2025-04-02 00:53 UTC

Citation for the original published paper (version of record):

Michael, A., Mark, A., Sasic, S. et al (2025). Generalized Langevin dynamics in multiphase direct numerical simulations using hydrodynamically optimized memory kernels. *Physics of Fluids*, 37(3). <http://dx.doi.org/10.1063/5.0254930>

N.B. When citing this work, cite the original published paper.

RESEARCH ARTICLE | MARCH 05 2025

# Generalized Langevin dynamics in multiphase direct numerical simulations using hydrodynamically optimized memory kernels <sup>EP</sup>

Special Collection: [250 Years of Brownian Motion](#)

Anand Joseph Michael ; Andreas Mark ; Srdjan Sasic ; Henrik Ström



*Physics of Fluids* 37, 033317 (2025)  
<https://doi.org/10.1063/5.0254930>



## Articles You May Be Interested In

Variance-reduced random batch Langevin dynamics

*J. Chem. Phys.* (December 2024)

On the non-stationary generalized Langevin equation

*J. Chem. Phys.* (December 2017)

Nondimensionalisations of the Langevin equation and small-parameter limits

*Physics of Fluids* (March 2025)

28 March 2025 08:59:02



Physics of Fluids  
Special Topics  
Open for Submissions

[Learn More](#)

# Generalized Langevin dynamics in multiphase direct numerical simulations using hydrodynamically optimized memory kernels

Cite as: Phys. Fluids **37**, 033317 (2025); doi: [10.1063/5.0254930](https://doi.org/10.1063/5.0254930)

Submitted: 25 December 2024 · Accepted: 6 February 2025 ·

Published Online: 5 March 2025



View Online



Export Citation



CrossMark

Anand Joseph Michael,<sup>1,a)</sup>  Andreas Mark,<sup>2</sup>  Srdjan Sasic,<sup>1</sup>  and Henrik Ström<sup>1</sup> 

## AFFILIATIONS

<sup>1</sup>Division of Fluid Dynamics, Chalmers University of Technology, Gothenburg, Sweden

<sup>2</sup>Department of Computational Engineering and Design, Fraunhofer-Chalmers Research Centre, Gothenburg, Sweden

Note: This paper is part of the Special Topic, 250 Years of Brownian Motion.

<sup>a)</sup> Author to whom correspondence should be addressed: [anandj@chalmers.se](mailto:anandj@chalmers.se)

## ABSTRACT

We propose a novel methodology for performing continuum-based simulations of Brownian motion in systems of arbitrary geometric complexity at thermal equilibrium. The methodology is valid for a wide range of particle-to-fluid density ratios,  $\rho_p/\rho_f = [1, 1000]$ . It is implemented in a multiphase direct numerical simulation framework, in which the complete hydrodynamic force acting on a particle can be obtained with high accuracy using the immersed-boundary method. The hydrodynamic force is then used with the particle velocity history in an optimization procedure, through which the hydrodynamic memory kernel can be established from a convolution integral without any *a priori* assumption about its functional form or scaling. The memory kernel is thereafter used to generate a colored Brownian force in agreement with the fluctuation–dissipation theorem. Finally, the hydrodynamic and Brownian forces are used to determine the particle acceleration, needed to evolve the particle trajectory, using the generalized Langevin equation. We show that the developed methodology correctly predicts the particle statistics in both unhindered and wall-adjacent Brownian motion, in good agreement with theoretical and experimental results. The current work, thus, lays the foundation for simulations of geometrically complex Brownian systems, where state-of-the-art multiphase techniques such as interface-capturing, turbulence modeling, heat and mass transfer, and chemical reactions can be accounted for. Furthermore, we discuss how the memory kernel, obtained on-the-fly as an integral part of the methodology, can potentially be used to correlate particle mobility with particle reactivity.

© 2025 Author(s). All article content, except where otherwise noted, is licensed under a Creative Commons Attribution (CC BY) license (<https://creativecommons.org/licenses/by/4.0/>). <https://doi.org/10.1063/5.0254930>

## I. INTRODUCTION

The seemingly random fluctuating motion of particles commonly referred to as Brownian motion is of significance in a wide range of fields such as surface-based reactors,<sup>1,2</sup> lab-on-chip devices,<sup>3</sup> soft matter physics,<sup>4</sup> microrheology,<sup>5</sup> microfluidics,<sup>1</sup> and biology.<sup>6</sup> These applications include artificial Brownian motors,<sup>7</sup> optical traps,<sup>8,9</sup> and biological ion channel flows,<sup>10</sup> to name a few. The study and development of these fields require an understanding of Brownian dynamics. Although experimental techniques are developing to enable better understanding of Brownian motion under various scenarios, they still struggle to accurately characterize Brownian motion. The minute length and time scales often associated with Brownian motion make accurate experimental tracking of such phenomena hard to achieve.<sup>11</sup> Simulation studies

offer an alternative method to analyze such minute systems at a lower cost and in more detail.

Numerous techniques have been developed over the years to simulate Brownian motion with varying degrees of success. Developing simulation models requires a description of the underlying physics involved with Brownian motion, which originates from molecular collisions. Molecules move around rapidly due to their thermal energy and collide with a Brownian particle imparting it some momentum, which results in Brownian motion over multiple molecular collisions whenever the particle inertia is small enough to allow it to respond to a temporal imbalance of collisions. Hence, an intuitive way to model Brownian motion is to use molecular simulations where individual molecules or clusters of molecules are simulated considering interparticle forces (often modeled as Lennard-Jones potential forces).<sup>12</sup>

Newtonian or Hamiltonian mechanics are used to model the change in velocity and position of the particles in the simulation based on the forces taken into consideration. The more accurate the force models considered, the better the simulation results.<sup>13</sup> The time scales of the simulation are restricted by the fastest occurring processes in the simulation, while the domain size of the simulation is restricted by the computational load of simulating multiple particles. The end result is that these simulations, although accurate at small scales and times, are difficult to extend to longer durations as well as larger domains.<sup>12,14</sup>

When observing Brownian motion at length and time scales much larger than molecular phenomena, it is convenient to describe the motion in terms of stochastic quantities. At larger time scales, the Brownian particle undergoes a large number of molecular collisions in a small period of time, providing it with a net momentum in a random direction. At the same time, the Brownian particle is also slowed down by molecular collisions that oppose its motion. Thus, at larger time scales, Brownian motion can be described as the combination of a random fluctuating force and a viscous damping force that tries to impede its motion, resulting in a random fluctuating motion for the particle.<sup>15</sup> In the Stokes limit, the classical Langevin equation (CLE) splits the Brownian motion into such a combination of a steady drag force (proportional to the particle velocity) and a random force.<sup>16</sup> Both these forces originate from the thermal fluctuations of molecules, and a relationship can be developed between the variance of the random force and the frictional force acting on the particle. This relationship, referred to as the fluctuation–dissipation theorem, is relatively straightforward to derive when the system is at thermal equilibrium.<sup>17</sup> Stokesian dynamics or Brownian dynamics simulations use the Langevin equation to depict Brownian motion as a combination of these forces,<sup>13,18</sup> with the random force modeled as a white-noise process.<sup>19,20</sup> The hydrodynamic force used in Stokesian dynamic simulations have been improved by using multiphase direct numerical simulation (DNS) approaches to simulate the fluid–particle interactions.<sup>15,21</sup> The reduced computational cost in these simulations allows for much larger domain and particle sizes. Simulations where the Brownian particle is much larger than the surrounding fluid are, therefore, often modeled using such approaches, where the frictional force is determined using some continuum approximation. While these simulations are good for revealing the long-term effects of Brownian motion, they fail to account for history effects in the development of the hydrodynamic boundary layers, which are significant when the density ratio of the Brownian particle is comparable to that of the surrounding fluid.<sup>22,23</sup> CLE-based methods are, therefore, limited to systems exhibiting high particle-to-fluid density ratios,<sup>19</sup> which effectively excludes many relevant systems where the fluid is a liquid and the particles are close to neutrally buoyant.

The generalized Langevin equation (GLE) is a modification of the classical Langevin equation that allows for the unsteady drag force (added mass and history effects) to be taken into account in addition to the steady drag force while modeling Brownian motion in a continuum description of the process.<sup>4</sup> The drag, added mass and history effects are often represented together as the convolution integral between a memory kernel and the velocity history of the particle. In this situation, the random

Brownian force can no longer be represented as a white-noise process, but instead requires a colored representation.<sup>22,24</sup> The fluctuation–dissipation theorem can still be used to generate a relation between the covariance of the colored random Brownian force and the memory kernel.<sup>25</sup>

Since the memory kernel is a continuum representation of molecular damping effects, there exist simulation techniques that derive the memory kernel from molecular dynamics simulations.<sup>14,26</sup> These methods, popularly referred to as coarse-graining techniques, often use the Mori-Zwanzig projection formalism to relate covariance functions generated from molecular dynamics quantities to memory kernels via Volterra equations<sup>27,28</sup> Volterra equation inversion techniques, as well as deep learning approaches, are used to solve these differential equations to obtain the hydrodynamic memory kernels.<sup>28–30</sup> These memory kernels are then used to generate the hydrodynamic forces as well as the random colored Brownian forces required to model Brownian motion using the GLE. However, as the GLE is still in the continuum regime, molecular simulations can be avoided altogether if the memory kernel can be derived from a hydrodynamic description instead. Such simulations would be less costly than molecular dynamics simulations and could still be used at low particle-to-fluid density ratios. Moreover, they would enable simulations of Brownian motion in industrially relevant systems that are challenging to describe with molecular approaches, such as diffusion in boundary layers influenced by large-scale turbulent structures and/or macroscopic phase interface undulations. Continuum-based simulation is, therefore, the approach taken in the current work.

It should be noted here that an alternate approach is represented by simulation techniques that rely on fluctuating the flow field instead of the particles to create the Brownian motion at all density ratios.<sup>31–33</sup> While these simulations give accurate particle physics, there are challenges associated with devising discretization schemes for the stochastic partial differential equations (because of the correlation between the form of the required fluctuation–dissipation relations and the choice of scheme,<sup>34</sup> the gridscale regularization (smoothing) of the stochastic forcing in finite-volume methods, and the integration of ill-behaved stochastic partial differential equations<sup>35</sup> where the notion of stability is different from that in regular deterministic schemes<sup>36</sup>). As we intend in our future work to utilize well-established methods for describing deterministic multiphase flows with evolving interfaces and chemical reactions, we have chosen to work with a GLE-based approach.

In this work, we, thus, develop a new method for simulating Brownian motion at thermal equilibrium in a continuum framework based on the GLE. We generate the memory kernel on-the-fly from a multiphase DNS description of the full hydrodynamic force acting on the particle, together with the particle velocity history, without any *a priori* assumption on the shape or scaling of the memory kernel in neither space nor time. The composition of the paper is as follows: we begin by reviewing the theoretical background to our methodology (Sec. II) and thereafter provide details on its numerical implementation (Sec. III). A number of simulation cases are defined (Sec. III F) and used to assess the performance of the method (Sec. IV). We show that the developed methodology accurately predicts the anomalous diffusion behavior of Brownian particles at low particle-to-fluid density ratios, while

exhibiting the correct scaling of the decay of the velocity autocorrelation function across a wide range of density ratios. Furthermore, we show that the methodology also intrinsically captures the expected modulation of the velocity autocorrelation due to the presence of a nearby solid surface. Finally, we present the particle memory kernel as obtained from our hydrodynamic optimizing procedure and discuss how it can be used to characterize the spatiotemporal environment surrounding a particle. The paper ends with conclusions and an outlook to the future (Sec. V).

## II. THEORY

The purpose of this section is to introduce the classical and generalized Langevin equations and the hydrodynamic memory kernel, along with the time scales of relevance in studies of Brownian motion using these descriptions.

The classical Langevin equation (CLE) is a well-established way to model the Brownian motion of a particle taking into account the steady drag force exerted by the surrounding fluid.<sup>16</sup> The CLE describes the force exerted on a particle that undergoes Brownian motion as the combination of a hydrodynamic drag force,  $\mathbf{F}_D(t)$ , and random Brownian force,  $\mathbf{F}_B(t)$ ,

$$m_p \frac{d\mathbf{V}(t)}{dt} = \mathbf{F}_D(t) + \mathbf{F}_B(t) = -\gamma\mathbf{V}(t) + \mathbf{F}(t). \quad (1)$$

Here,  $m_p$  refers to the mass of the particle, and  $\mathbf{V}(t)$  is the velocity of the particle at time  $t$ . Since the drag force is proportional to the velocity of the particle, it is represented as the combination of a drag coefficient,  $\gamma$ , and the particle velocity.

The fluctuation–dissipation theorem for a system at equilibrium gives that the autocovariance of the random Brownian force is proportional to the drag coefficient,<sup>4,22,24</sup>

$$\langle F_{Bi}(t - \tau)F_{Bj}(\tau) \rangle = 2k_B T \gamma \delta_{ij} \delta(\tau). \quad (2)$$

Here,  $k_B$  is the Boltzmann constant,  $T$  is the absolute temperature, and  $\tau$  is a time lag. The subscripts  $i$  and  $j$  in Eq. (2) are used to represent the orthogonal directions in a three-dimensional space. This equation, thus, shows that the Brownian force has only an instantaneous covariance in time, represented by the Dirac delta function,  $\delta(\tau)$ , which allows it to be modeled as a Markovian white-noise process in simulations.<sup>15,19,20</sup>

Assuming that the system is at thermal equilibrium, that the equipartition theorem holds (so that  $\langle V(t)^2 \rangle = k_B T / m_p$ ), and that the Brownian force is uncorrelated to the particle velocity, the velocity autocorrelation decay for an unhindered particle developed using the CLE becomes<sup>4,22</sup>

$$\frac{\langle V(0)V(t) \rangle}{\langle V(0)^2 \rangle} = \exp\left(-\frac{\gamma t}{m_p}\right). \quad (3)$$

Furthermore, the particle diffusivity,  $D$ , is obtained as

$$D = \int_0^\infty \frac{k_B T}{m_p} \exp\left(-\frac{\gamma t}{m_p}\right) dt = \frac{k_B T}{\gamma}. \quad (4)$$

The time scale entering Eqs. (3) and (4) is the particle response time,  $\tau_p = m_p / \gamma$ . This time scale characterizes the response of the particle to external stimuli. In an unhindered scenario for a spherical

particle,  $\gamma = 6\pi\mu r_p$ ,<sup>37</sup> where  $r_p$  is the radius of the particle, and  $\mu$  is the viscosity of the fluid. If the particle mass is also expressed in similar terms as  $m_p = \frac{4}{3}\pi r_p^3 \rho_p$ , then the particle response time can be written as  $\tau_p = \frac{2}{9} r_p^2 \rho_p / \mu$ . The viscous effects from the fluid propagate over the particle at a time scale  $\tau_f = r_p^2 \rho_f / \mu = r_p^2 / \nu$  (where  $\nu = \mu / \rho_f$  is the kinematic viscosity of the fluid). In a situation where a particle is situated close to a solid wall, the time scale  $\tau_w = h^2 / \nu$ , where  $h$  is the distance between the center of the particle and the surface of the wall, characterizes the time when the particle-induced vorticity reaches the surface and one can expect to see influences on the particle motion due to the presence of the wall. Similarly, the time scale  $\tau_A = L^2 / \nu$ , where  $L$  is the domain size, represents when finite-size effects start to manifest in a simulation aimed at mimicking an unbounded scenario.<sup>32,38</sup>

When the particle density is much higher than the fluid density, the particle response time is much larger than the fluid response time (i.e.,  $\tau_p / \tau_f = \frac{2\rho_p}{9\rho_f} \gg 1$ ). At such time scale ratios, the fluid history effects have a negligible impact on the particle as they act on time scales much smaller than the particle response time. The hydrodynamic force on the particle can be considered to be only the steady drag in such a case, and the CLE is a valid model. However, when the particle density is close to the fluid density ( $\tau_p / \tau_f = \frac{2\rho_p}{9\rho_f} \approx 1$ ), the unsteady drag (added mass and history effects) operates on time scales comparable to the particle response time. The CLE and its associated fluctuation–dissipation theorem are no longer an accurate model for the Brownian motion of a particle at such low solid–fluid density ratios, as the hydrodynamic force has significant contributions from the added mass and history effect apart from the steady drag.<sup>23</sup>

The generalized Langevin equation (GLE) is a modification to the CLE that accounts for the added mass and history effects in addition to the steady drag

$$m_p \frac{d\mathbf{V}(t)}{dt} = \mathbf{F}_H(t) + \mathbf{F}_B(t) = - \int_0^t \mathbf{K}(t, \tau) \cdot \mathbf{V}(t - \tau) d\tau + \mathbf{F}_B(t). \quad (5)$$

The dissipative hydrodynamic force,  $\mathbf{F}_H(t)$ , in the GLE is represented as a convolution integral between a memory kernel tensor,  $\mathbf{K}(t, \tau)$ , and the complete velocity history of the particle. The components of the total hydrodynamic force in each direction are influenced by the history of the motion of the particle in all three orthogonal directions,<sup>25</sup>

$$F_{H,i}(t) = - \int_0^t K_{ij}(t, \tau) V_j(t - \tau) d\tau. \quad (6)$$

The memory kernel can, thus, be thought of as carrying information about the spatial and temporal history of the particle motion at a time lag of  $\tau$  from the instance  $t$ , as can be seen from its multi-dimensional representation which correlates the velocity history of the particle with the current hydrodynamic force. In other words, the memory kernel  $\mathbf{K}(t, \tau)$  at any instance  $t$  has values that correspond to the velocity of the particle at time  $\tau$  in the past from the current time. A theoretical estimation of the hydrodynamic memory kernel for a sphere in an unhindered scenario is<sup>24</sup>

$$K_{ij}(t, \tau) = \begin{cases} \gamma \left( 2\delta(\tau) - \sqrt{\tau_f} \frac{\tau^{-3/2}}{2\sqrt{\pi}} \Theta(\tau) \right), & \text{if } i = j, \\ 0, & \text{if } i \neq j, \end{cases} \quad (7)$$

where  $\Theta(t)$  is the Heaviside step function. Here, the symmetry of the sphere and unhindered nature of the surrounding domain reduce the non-diagonal terms of the memory kernel to zero. The unhindered domain also makes the memory kernel independent of instance  $t$  when it is estimated and the values only depend on the time lag  $\tau$ .

Applying the fluctuation–dissipation theory to the GLE and assuming the system is at equilibrium gives a relation between the memory kernel and the random Brownian force, as shown in the following equation:

$$\langle F_{B,i}(t - \tau)F_{B,j}(t) \rangle = k_B T K_{ij}(t, \tau). \quad (8)$$

The covariance of random Brownian forces separated by a certain lag time ( $\tau$ ) is proportional to the memory kernel value at those lag times. At any instance of time, the three-dimensional memory kernel tensor accounts for the autocovariance,  $\langle F_{B,i}(t - \tau)F_{B,i}(t) \rangle = k_B T m_p K_{ii}(t, \tau)$ , as well as the cross-covariances,  $\langle F_{B,i}(t - \tau)F_{B,j}(t) \rangle = k_B T m_p K_{ij}(t, \tau)$  (where  $i \neq j$ ), of the Brownian forces. Hence, the random Brownian forces used in the GLE can no longer be modeled as a Markovian white-noise process and instead requires a colored non-Markovian approach that accounts for the changing force covariance in time.

The theoretical understanding of the GLE and its associated fluctuation–dissipation relation has been used to develop a novel multiphase DNS approach to modeling Brownian motion incorporating memory effects. The memory kernel obtained as part of this method can also be analyzed directly to provide insight into the evolution of the spatiotemporal environment surrounding individual particles. This method is described in detail in the next section.

### III. NUMERICAL METHODOLOGY

The aim of the current work is to derive a novel methodology that develops the memory kernel from the hydrodynamic force acting on the Brownian particle in a continuum framework using Eq. (6). The memory kernel is then used to generate the colored Brownian force based on the fluctuation–dissipation relation as stated in Eq. (8).

The numerical method used to obtain the memory kernel and model the Brownian motion using the GLE consists of four main steps:

1. Find the hydrodynamic force acting on the particle.
2. Obtain the memory kernel via an optimization procedure, from knowledge of the current hydrodynamic force, the velocity history of the particle, and their relation via a convolution integral.
3. Use the memory kernel found to generate a colored Brownian force in agreement with the fluctuation–dissipation theorem.
4. Employ the hydrodynamic and Brownian forces in the determination of the particle acceleration, using the generalized Langevin equation.

The implementation of the numerical method will be further detailed throughout this section. An overview is provided in Algorithm 1.

#### ALGORITHM 1: Pseudo-code of proposed methodology.

- 
- 1: **Initialize** (at time  $t = 0$ ): Memory kernel  $K_i$  as array of size  $N$  with all terms set to zero; velocity  $\mathbf{V}$ , position  $\mathbf{X}$ , hydrodynamic force  $\mathbf{F}_H$  as zero vectors; Brownian force  $\mathbf{F}_B$  using equation 27
  - 2: Initiate motion of the particle (equation 19)
  - 3: **for**  $t = 0$  to  $T$  **do**
  - 4: Calculate the hydrodynamic force ( $\mathbf{F}_H$ ) (equation 11 or 12)
  - 5: **if**  $t < N\Delta t$  where  $\Delta t$  is the time step **then**
  - 6: Pass  $\mathbf{F}_H$ , last  $n = t/\Delta t$  terms of  $\mathbf{V}$ , and current values of the first  $n$  terms of  $K_i$  as initial guess for the optimization routine
  - 7: Optimize the first  $n$  terms of the memory kernel by minimizing the cost function (equation 14)
  - 8: **else**
  - 9: Pass  $\mathbf{F}_H$ , last  $N$  terms of  $\mathbf{V}$ , and current values of all the  $N$  terms of  $K_i$  as initial guess for the optimization routine
  - 10: Optimize the whole memory kernel by minimizing the cost function (equation 14)
  - 11: **end if**
  - 12: From memory kernel, create covariance matrix of Brownian force (equation 15)
  - 13: **if** covariance matrix is positive semi-definite (PSD) **then**
  - 14: Factorize covariance matrix into root matrices (equation 16)
  - 15: Generate Brownian force ( $\mathbf{F}_B$ ) by multiplying root matrix with series of normal random numbers (equations 17 and 18)
  - 16: Use GLE to move the particle (equation 19)
  - 17: Store current particle velocity for use in the optimization routine
  - 18: **else**
  - 19: Redo steps 5–11 including PSD condition as a constraint
  - 20: **end if**
  - 21: **end for**
- 

#### A. The hydrodynamic force

We shall assume in the following that the memory kernel tensor is diagonal. The memory kernel has been proven symmetric for particles of arbitrary shape,<sup>25</sup> meaning that there are never more than six independent components in the  $3 \times 3$  tensor. In anisotropic geometries or at finite Reynolds numbers, the off diagonal (cross-covariance) terms in the kernel could become non-zero, but under the current conditions, i.e., the spherical shape of the particle as well as the symmetry of the domains in which the simulations for this work have been carried out, they should be negligible.<sup>39,40</sup> It is then beneficial to remove them in the optimization procedure (to be described in Sec. III B) to limit the impact of numerical noise on the optimization. Consequently, it is expected that in anisotropic particle or domain geometries, these terms may be included without adverse effects whenever they are significant. Here, however, we let  $K_{ij} = \delta_{ij}K_{ii}$ .<sup>26</sup> In an unhindered setting, it is then sufficient to discuss  $K(t)$ , whereas the diagonal tensor is split into normal ( $\perp$ ) and parallel ( $\parallel$ ) components

for hindered configurations.<sup>39,40</sup> The hydrodynamic force can then be restated so that the force is only dependent on the velocity history along the same direction,

$$F_{H,i} = - \int_0^t K_i(t, \tau) V_i(t - \tau) d\tau. \quad (9)$$

The corresponding Brownian force covariance derived from the fluctuation–dissipation theorem becomes

$$\langle F_{B,i}(t - \tau) F_{B,j}(t) \rangle = k_B T K_{ij}(t, \tau) \delta_{ij}. \quad (10)$$

The hydrodynamic force acting on the Brownian particle can be determined in different ways depending on the multiphase simulation method used to simulate the fluid system in which the particle is immersed. In the case of conventional Lagrangian particle tracking (LPT) methods, the force exerted by the fluid on the particle is mathematically modeled. Mathematical models for the fluid force have only been developed for certain cases and are generally not available for geometrically complex systems. When the particle is spherical and its motion is unhindered, the hydrodynamic force in the limit  $Re_p = 2r_p |\mathbf{V}|/\nu \rightarrow 0$  (where  $Re_p$  is the particle Reynolds number) may be modeled as<sup>4,22,24,41</sup>

$$\mathbf{F}_H(t) = -\gamma \mathbf{V}(t) - \frac{2}{3} \pi r_p^3 \rho_f \frac{d\mathbf{V}(t)}{dt} - \gamma r_p \int_0^t \frac{d\mathbf{V}(\tau)}{d\tau} \frac{d\tau}{[\pi \mu(t - \tau)/\rho_f]^{1/2}}. \quad (11)$$

Here, the first term on the right-hand side of Eq. (11) is the steady drag force and the two other terms are the unsteady drag contributions (the added mass force and the history force in that order). Note that if the background fluid is not quiescent,  $\mathbf{V}(t)$  should be replaced by  $\mathbf{V}(t) - \mathbf{U}(t)$ , where  $\mathbf{U}(t)$  is the fluid velocity interpolated to the location of the particle centroid if the particle were not there.<sup>41</sup>

In more general flow scenarios where mathematical models for  $\mathbf{F}_H(t)$  are not yet available, the fluid force on the particle must instead be calculated from a surface integral of the pressure,  $p$ , and viscous stress fields,  $\tau_{ij}$ , acting on the particle surface,  $S$ , as shown in the following equation:

$$\begin{aligned} \mathbf{F}_H(t) &= \int_S (-p \delta_{ij} + \tau_{ij}) n_j dS, \\ &= \int_S \left( -p \delta_{ij} + \mu \left( \frac{\partial u_i}{\partial x_j} + \frac{\partial u_j}{\partial x_i} \right) \right) n_j dS. \end{aligned} \quad (12)$$

The pressure and velocity fields surrounding the particle required for the stress calculation can be determined by numerically solving the Navier–Stokes equations. While there are many multiphase simulation techniques available for such calculations, the immersed boundary method with fluid structure interaction (IB-FSI) has been implemented using the IBOFlow software in this work to get such a numerical solution for the pressure and velocity fields and then determine the hydrodynamic force on the particle.<sup>42</sup> It should be stressed here that the availability of the fully resolved velocity and pressure fields everywhere in the continuous phase allows for a model-free determination of all hydrodynamic interactions between particles as well as between particles and system boundaries. The numerical aspects of the IB-FSI method are further discussed in Sec. III E.

In both the LPT and the IB-FSI frameworks used in the current work, the fluid is assumed to be incompressible. This assumption implies that phenomena occurring faster than  $\tau_s = r_p/s$ , where  $s$  is the speed of sound in the fluid, are instantaneous in the current description.<sup>38</sup> Although this assumption is not an integral part of the developed framework and, thus, can be avoided with a fully compressible description of the hydrodynamics, it should be emphasized that the asymptotic decay studied in the present work does not depend on the incompressibility assumption.<sup>25</sup>

### B. The memory kernel

Once the hydrodynamic force acting on a particle at a time instance has been determined, the memory kernel is determined by applying optimization procedures to Eq. (9) since the velocity history of the particle can also be tracked as part of the simulation process. Although multiple optimization procedures are available, in this work the implementation of the limited-memory Broyden–Fletcher–Goldfarb–Shanno optimization routine (L-BFGS-B)<sup>43–45</sup> from the `scipy` python library<sup>46</sup> is used to estimate the memory kernel.

Since the hydrodynamic force will be equal to the convolution integral of the memory kernel and the velocity history, a cost function for the optimization routine,  $C$ , can be derived by taking all the terms in Eq. (9) to one side,

$$C(K_i(t, \tau)) = \frac{|F_{H,i}(t) + \int_0^t K_i(t, \tau) V_i(t - \tau) d\tau|}{|F_{H,i}(t)|}. \quad (13)$$

The equation for the cost function can be discretized for numerical implementation by dividing the total time,  $t$ , over which the velocity history has been recorded, into  $N$  intervals such that  $t = n\Delta t$ , where  $n = 0$  to  $N$ ,

$$C(K_i(t, \tau)) = \frac{\left| F_{H,i}(t) + \sum_{n=0}^N K_i(t, n\Delta t) V_i(t - n\Delta t) \Delta t \right|}{|F_{H,i}(t)|}. \quad (14)$$

The optimization routine starts with initial guess values for the memory kernel in a particular direction,  $K_i(t, \tau)$ , corresponding to each value of  $\tau = n\Delta t$  where  $n = 0$  to  $N$ . Thus, the memory kernel has  $N$  values that need to be optimized using the last  $N$  terms of the velocity history of the particle as depicted in the discretized cost function [Eq. (14)]. The hydrodynamic force in the same direction,  $F_{H,i}$ , is the fluid force exerted on the particle determined either using the model [Eq. (11)] or the stress integral [Eq. (12)] as discussed previously. The convolution integral of the guessed memory kernel and the velocity history is then used to calculate the fluid force using the discretization shown in the second term of Eq. (14). The cost function is, thus, the difference between the numerically estimated hydrodynamic force,  $F_{H,i}$ , and the memory-kernel-based estimation of the hydrodynamic force. The optimization routine then iteratively modifies the memory kernel to minimize the cost function below a certain threshold ( $10^{-6}$  in our simulations). The procedure is run three times to determine the memory kernel in all three directions. The converged memory kernel is then passed on to the next part of the simulation routine used to determine the random colored Brownian force in each direction.

The memory kernel is initialized as a zero tensor at the beginning of the simulation. A completely random force is used to initiate the motion of the particle at the very first time step with its variance proportional to the white-noise equivalent for the same Brownian particle at the particle-fluid density ratio used in the simulation [given later as Eq. (27)]. At all subsequent time steps, the random force is determined based on the memory kernel developed so far. The memory kernel is gradually built up and extended over the course of a simulation, with each time step of the simulation adding a new term to the kernel in each direction. All the values in the memory kernel are optimized simultaneously. The values of the terms in the memory kernel developed in the previous time step are used as an initial guess for the determination of the current memory kernel. In order to accurately determine the peaks and valleys in the kernel corresponding to large and small terms, in the initial few time steps of the simulation, the memory kernel is fit to not just the current hydrodynamic force on the particle but also to the hydrodynamic force at five time steps in the recent past, along with their associated velocity histories. Here, the memory kernel is assumed to remain relatively the same over multiple time steps as the particle shifts do not significantly change the geometric neighborhood of the particle at each time step.

### C. The Brownian force

The fluctuation–dissipation relation for the GLE relates the random Brownian force used in the GLE to the hydrodynamic memory kernel. This relation can, thus, be used to generate the colored random Brownian force for the GLE-based simulation. The first step in the generation of the random force is to generate the covariance matrix in time for the random force from the memory kernel estimated using the optimization routine. Based on the fluctuation–dissipation relation [Eq. (10)], the discretized memory kernel terms can be arranged in a square  $N \times N$  matrix (where  $N$  is the number of terms in the memory kernel) to generate the covariance matrix,

$$\begin{aligned} \text{Cov}(F_{B,i})_{N,N} &= [(F_{B,i}(t - n\Delta t)F_{B,i}(t))]_{N,N}, \\ &= k_B T [K(t, n\Delta t)]_{N,N}, \\ &= k_B T \begin{bmatrix} K(t, 0) & K(t, \Delta t) & \dots & K(t, N\Delta t) \\ K(t, \Delta t) & K(t, 0) & \ddots & \vdots \\ \vdots & \ddots & \ddots & K(t, \Delta t) \\ K(t, N\Delta t) & \dots & K(t, \Delta t) & K(t, 0) \end{bmatrix}. \end{aligned} \tag{15}$$

The diagonal terms in the covariance matrix depict the variance of the random force. The non-diagonal terms of the matrix characterize the covariance of the random force terms separated by certain time ( $n\Delta t$ ). The further the term is from the diagonal, the further apart the correlated random forces are in time as well.

Since covariance matrices are positive semidefinite (PSD), it is essential to ensure that the memory kernel determined from the optimization routine produces a PSD covariance matrix.<sup>26</sup> If this is not the case, the optimization routine is rerun using a Trust Region method known in the `scipy` library as the `trust-constr` routine to enforce this property.<sup>47</sup> The constraint incorporates a function that checks if the covariance matrix generated from the current iteration of

the memory kernel satisfies the PSD condition (i.e., that it only has non-negative eigenvalues). If the constraint is not satisfied, the magnitude of the negative eigenvalues are used to penalize the optimization routine and steer the optimization routine toward a kernel that can give a covariance matrix that satisfies the PSD condition. As the constrained optimization is slower, it is more computationally efficient to work without constraints unless required. Therefore, the optimization routine usually works with the L-BFGS-B method without constraints and only uses the Trust Region method with constraints when the covariance matrix does not satisfy the PSD condition. The initial guess for the constrained optimization is the previously fitted memory kernel obtained from the L-BFGS-B method.

The positive semidefinite covariance matrix  $\text{Cov}(F_{B,i})_{N,N}$  can be factorized using Cholesky decomposition into triangular root matrices  $L_{N,N}$  and its transpose  $L_{N,N}^T$ ,

$$\text{Cov}(F_{B,i}) = L_{N,N} L_{N,N}^T. \tag{16}$$

The lower triangular matrix  $L_{N,N}$  can be multiplied with a series of  $N$  normally distributed random numbers  $\mathcal{N}(0, 1)_{N,1}$  of mean 0 and variance 1 to produce a series of random Brownian forces  $F_{N,1}$ ,

$$[F]_{N,1} = [L]_{N,N} [\mathcal{N}(0, 1)]_{N,1}. \tag{17}$$

The vector  $F_{N,1}$  is, thus, a series of random forces that have the same covariance as the memory kernel, thereby satisfying the fluctuation–dissipation relation for the GLE. The last term of the random number force series,  $F_{N,1}[N]$ , is chosen as the Brownian force for the next step in the GLE,

$$F_{B,i}(t) = [F]_{N,1}[N]. \tag{18}$$

The random number series used to generate the Brownian force has the same number of terms as the memory kernel. At each new time step, a new random number is added at one end of the series, while a number is deleted from the other end to ensure that the random Brownian force keeps changing at each time step while maintaining a constant memory kernel size. The rotation through the series of the random numbers when multiplied with the root of the covariance matrix ensures that the Brownian force series follows the correct covariance relationship as specified by the memory kernel, thereby making sure that the fluctuation–dissipation relationship is satisfied.

### D. The generalized Langevin equation

The hydrodynamic force,  $F_H(t)$ , and the newly determined random colored force,  $F_B(t)$ , can now be used in the GLE to determine the acceleration of the particle,

$$\mathbf{a}(t) = \frac{\mathbf{F}_H(t) + \mathbf{F}_B(t)}{m_p}. \tag{19}$$

The following time-stepping sequence is used to estimate the particle velocity and position at the next time step in the LPT framework ( $\Delta t$  is the time step size),

$$\mathbf{V}(t + \Delta t) = \mathbf{V}(t) + \mathbf{a}(t)\Delta t, \tag{20}$$

$$\mathbf{X}(t + \Delta t) = \mathbf{X}(t) + \mathbf{V}(t)\Delta t + \mathbf{a}(t) \frac{\Delta t^2}{2}. \tag{21}$$

In the IB-FSI framework, the following time-stepping sequence is used instead,<sup>48</sup>

$$\mathbf{V}(t + \Delta t) = \mathbf{V}(t) + \frac{\Delta t}{2} [\mathbf{a}(t) + \mathbf{a}(t + \Delta t)], \quad (22)$$

$$\mathbf{X}(t + \Delta t) = \mathbf{X}(t) + \mathbf{V}(t)\Delta t + \frac{\Delta t^2}{2} [\mathbf{a}(t)]. \quad (23)$$

Here  $\mathbf{a}(t + \Delta t)$  is an implicit acceleration that is iteratively determined assuming that the force balance holds between the hydrodynamic force and the current Brownian force at the future position obtained based on Eqs. (22) and (23). Note that these schemes are both compliant with the Itô interpretation<sup>49</sup> of a stochastic integral.

To summarize, the simulation process for the Brownian motion, thus, begins with the determination of the hydrodynamic force,  $\mathbf{F}_H$ , acting on the particle. The hydrodynamic memory kernel,  $\mathbf{K}(t, \tau)$ , is determined by optimizing it based on the hydrodynamic force utilizing the velocity history,  $\mathbf{V}(t)$ , of the particle. The fitted memory kernel is then used to create the covariance matrix for the random Brownian force, which is factorized into its root matrices and multiplied with a normal random variable series to generate the Brownian force,  $\mathbf{F}_B$ . The Brownian force, along with the hydrodynamic force on the particle, are used to move the particle for a single time step using the GLE. This sequence of steps is repeated at every time level, to get the current hydrodynamic force, the memory kernel and a new random Brownian force at the new particle position.

### E. Numerical considerations

The time step used in the integration of the GLE is set to  $\Delta t = \tau_p/50$ , so that the acceleration of the particle is sufficiently well resolved.<sup>15</sup> Although the memory kernel will ideally keep growing as long as the particle is moving by adding one new term for each time step, its length here is limited to correspond to  $10\tau_p$  to optimize the use of computational time and memory. This choice means that the simulation does not track memory effects beyond  $10\tau_p$  into the history of the particle motion. The terms in the memory kernel have been observed to become negligibly small ( $|\mathbf{K}(t, \tau > 10\tau_p)|/\max|\mathbf{K}(t, \tau)| < 10^{-5}$ ) beyond this point in time, so as to not contribute significantly to the colored force generation. Therefore, ignoring these terms in the simulation have been assumed to not significantly influence the results, as it is also known that previous works have employed even shorter memory kernels (e.g.,  $2.5\tau_p$  in Ref. 26). The computational time was observed to increase linearly with the memory kernel size, so a finite cutoff length ensures shorter simulation times for each individual time step.

In all simulations, the particle trajectories are evolved using Eqs. (19)–(23), depending on the framework used. In the LPT approach, the hydrodynamic force is discretized in time as

$$\mathbf{F}_H(t) = -\gamma\mathbf{V}(t) - \frac{1}{2}m_p\frac{\rho_f}{\rho_p}\mathbf{a}(t) - \gamma\Delta t\sqrt{\frac{r_p^2\rho_f}{\pi\mu}}\sum_{\tau=0}^{\tau=t-\Delta t}\frac{\mathbf{a}(\tau)}{(t-\tau)^{1/2}}. \quad (24)$$

Here, the particle acceleration  $\mathbf{a}(t)$  is determined using information from time levels  $t$  and  $t - \Delta t$ .

In the IB-FSI method, the hydrodynamic force on the particle is instead calculated as the surface integral of the pressure and viscous

stresses acting on the particle using Eq. (12). This calculation involves solving the Navier–Stokes equations,

$$\frac{\partial u_j}{\partial x_j} = 0, \quad (25)$$

$$\rho_f\left(\frac{\partial u_i}{\partial t} + u_j\frac{\partial u_i}{\partial x_j}\right) = -\frac{\partial p}{\partial x_j} + \mu\frac{\partial^2 u_i}{\partial x_j^2}. \quad (26)$$

This set of equations is solved numerically in a finite-volume framework together with the implicit Dirichlet immersed-boundary (IB) condition  $u_i = u_i^{IB}$ . The coefficients obtained from the discretization of the Navier–Stokes equations are closed with a second-order accurate interpolation that arises from this condition employed at the IB-fluid interface. The mirroring immersed-boundary method employed<sup>42,50</sup> mirrors the velocity over the IB to a velocity point in the flow domain. The velocity field at the interior cell centers of the IB is set so that a linear interpolation between that cell center and the velocity at the fictitious cell center is exactly the implicit Dirichlet IB condition. The fictitious reversed velocity field inside the IB generated by the IB condition is excluded when calculating fluid fluxes in the momentum equation and pressure equation source terms. The pressure is also not solved for cells inside the IB and pressure gradients are extrapolated over the IB interface.

The domain used in the IB-FSI simulations is a cube with a side length of  $30r_p$ . The boundaries in the  $x$  and  $y$  directions are set as walls. In the  $z$ -direction, the bottom boundary is set to a wall, while the top boundary was set as pressure outlet with a static gauge pressure of 0 Pa. The domain is discretized with a base cell size of  $2.5r_p$  and with a finer resolution of  $\frac{5}{128}r_p$  at the boundaries. The time step of  $\frac{1}{50}\tau_p$  along with this refinement in grid size was shown to be sufficient to get grid and time step convergence in the simulation of a settling particle in a previous study using the same method,<sup>15</sup> and new grid and time step studies conducted for this work (not shown) yielded similar conclusions.

### F. Simulation cases

The GLE-based algorithm described above has been tested by simulating the Brownian motion of a spherical particle in different environments. The problem is made dimensionless by the use of  $r_p$  as the characteristic length scale,  $\tau_p$  as the time scale, and  $V_{rms} = \sqrt{k_B T/m_p}$  [the root mean square (RMS) velocity] as the velocity scale. The governing dimensionless parameters are then the particle Reynolds number,  $Re = 2r_p V_{rms}/\nu$ , and the particle-to-fluid density ratio  $\rho_p/\rho_f$ . We probe density ratios in the range 1–1000 in our simulations, and consequently, the Reynolds number varies within the range  $Re = [4.45 \times 10^{-7}, 4.45 \times 10^{-4}]$ , which is considered relevant for many applications.<sup>40</sup>

Two types of domain are simulated to showcase the capabilities of the method proposed in this work. In the first type, a Brownian particle is simulated in an unhindered scenario where the particle has no solid objects (other particles or walls) in its close neighborhood. In the second type, the particle is positioned adjacent to a wall, which influences the hydrodynamic response, and thus, its Brownian motion.

#### 1. Unhindered case

The unhindered case was simulated at four different density ratios using three methods:

- LPT with memory-kernel-based GLE
- IB-FSI with memory-kernel-based GLE
- LPT with CLE (no memory effects)

The hydrodynamic force acting on the Brownian particle in the LPT approaches is obtained using Eq. (11). In the IB-FSI approach, it is obtained using Eq. (12), and the unbounded setting is represented by placing the particle at the domain center far ( $15r_p$ ) from all domain boundaries.

In the LPT-based simulation where the particle is moved using CLE modeling (as a base point to highlight the improvements that GLE-based method brings to the simulation results), the Brownian force is modeled as a normally distributed white-noise process with no memory effects.<sup>15,19,20</sup> In these simulations, the force is modeled based on the fluctuation–dissipation relation in Eq. (2) according to

$$F_{B,i} = \sqrt{\frac{2k_B T \gamma}{\Delta t}} \mathcal{N}(0, 1). \tag{27}$$

While the particle density was maintained constant at  $1000 \text{ kg/m}^3$ , the fluid density is changed from 1 to  $1000 \text{ kg/m}^3$  in multiples of 10 to produce a change in the particle-density ratio ( $\rho_p/\rho_f$ ) going from 1 (characteristic of liquid-phase systems) to 1000 (characteristic of gas-phase systems). The variation in the density ratio was done to show how the behavior of the particle is affected by the added mass and history effects that are significant at particle-to-fluid density ratios close to 1. The unhindered case setup is detailed in Fig. 1.

**2. Wall-adjacent case**

In the wall-adjacent case, the Brownian motion of the same particle is simulated close to a wall. This simulation is performed to demonstrate the applicability of the method to more general flow scenarios where there are solid boundaries from other particles and/or domain features present. These domain features, such as the wall considered in

this case, alter the hydrodynamic force experienced by the particle from that in an unhindered scenario. It is relatively easier to obtain the hydrodynamic force in general flow scenarios using the IB-FSI framework compared to the LPT framework. Mathematical models for the total hydrodynamic force are not available in the LPT framework for cases of arbitrary geometric complexity. Thus, wall-adjacent simulations are performed using only the IB-FSI framework.

The domain used in the IB-FSI framework for these cases has the same dimensions as before, but the particle is now placed with its center at a distance of  $1.25r_p$  from the wall previously mentioned in the  $z$ -direction. Since the particle is still in the center of the domain in the  $x$  and  $y$  directions, the effects from the boundaries in these directions can be considered negligible. In this case, the particle-to-fluid density ratios of 1 and 10 are simulated. The setup is illustrated in Fig. 2.

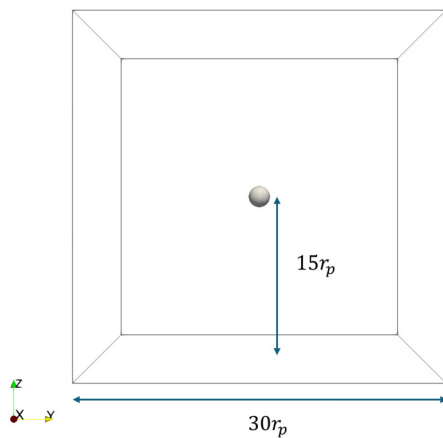
**G. Characterizations of Brownian motion**

In each of the simulations performed, the particle position and velocity are recorded to develop the mean square displacement (MSD) and the velocity auto-correlation function (VACF) at different lag times. Brownian motion at the continuum level is depicted as a statistical phenomenon, and hence, the behavior of a particle undergoing this random motion is described in terms of statistical averages. The MSD is a measure of how quickly a particle diffuses or moves away from its original position due to Brownian motion. The VACF, on the other hand, depicts how quickly the velocity of the particle becomes uncorrelated from its initial value and can be thought of as how quickly the particle forgets its initial velocity.

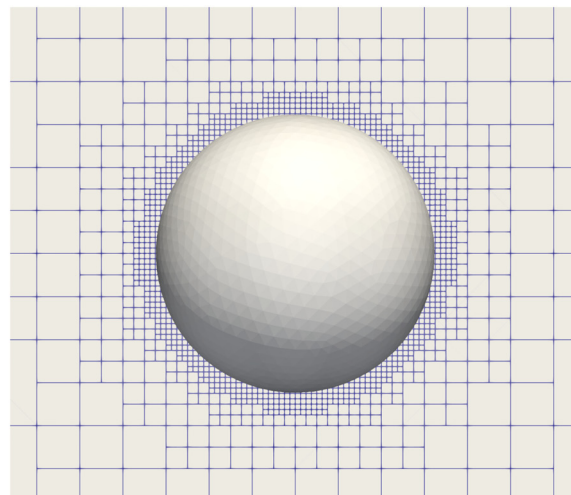
The MSD is calculated from the particle position data,

$$\langle X^2(t) \rangle = \langle \Delta X^2(\Delta t) \rangle = \frac{1}{M} \sum_{t=0}^{t=T-\Delta t} [X(t + \Delta t) - X(t)]^2. \tag{28}$$

Similarly, the VACF is calculated from the particle velocity data,



(a) Setup



(b) Grid Discretisation

**FIG. 1.** The unhindered case setup is depicted in (a). The particle is placed at the center of the domain with a distance of  $15r_p$  between the particle center and the walls, which makes any effect from the walls negligibly small. In (b), the grid discretization used in the IPS-FSI framework simulation is shown. The smallest cells have a size of  $5r_p/128$ .

28 March 2025 08:59:02

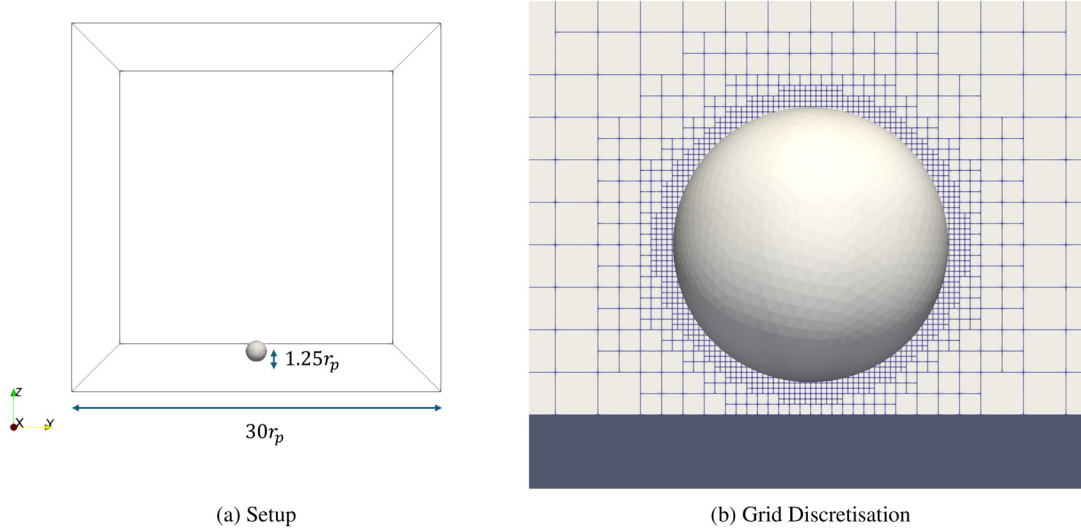


**FIG. 2.** The wall-adjacent case setup is shown in (a). The particle is placed with its center at a distance of  $1.25r_p$  from the wall in the  $z$ -direction so that the changes in the particle behavior due to the presence of the wall can be observed. In (b), the grid discretization used in the IPS-FSI framework simulation is shown. The smallest cells have a size of  $5r_p/128$ .

$$C_V(\Delta t) = \langle V(0) \cdot V(\Delta t) \rangle = \frac{1}{M} \sum_{t=0}^{t=T-\Delta t} [V(t) \cdot V(t + \Delta t)]. \quad (29)$$

In Eqs. (28) and (29),  $M$  is the total number of data points,  $T$  is the total time, and the lag time refers to the time difference  $\Delta t$  by which the two values used in MSD and VACF calculations are separated. The simulations are run for a total of  $1000\tau_p$  in each case to ensure that there are enough samples of the particle position and velocity to obtain stable MSD and VACF values up to a lag time of at least  $\tau_p$ . The results will be shown up to  $5\tau_p$  for the VACF and  $10\tau_p$  for the MSD.

The MSD and VACF values obtained at different density ratios from these simulations will be compared with their corresponding theoretical values. Analytical solutions for the MSD and the VACF at different time lags for a particle undergoing unhindered Brownian motion defined by the GLE were obtained by Mainardi *et al.*<sup>22</sup> When the added mass effect is considered in the GLE, the effective mass of the particle including the fluid it drags with it becomes  $m_e = m_p(1 + \rho_f/2\rho_p)$  in the unhindered case. The effective particle response time then becomes  $\tau_e = \tau_p(1 + \rho_f/2\rho_p)$ . In this situation, the MSD can be represented as

$$\langle X^2(t) \rangle = 2dD \left\{ t - 2\sqrt{\frac{\beta\tau_e t}{\pi}} + \frac{a_+^3 [1 - E_{1/2}(a_-\sqrt{t})] - a_-^3 [1 - E_{1/2}(a_+\sqrt{t})]}{(a_+ - a_-)(a_+ a_-)^2} \right\}. \quad (30)$$

Here,  $d$  is the dimension of the system ( $d=3$  in the cases discussed here, since they are three-dimensional),  $D = k_B T/\gamma$  is the diffusion coefficient for the particle while  $\beta = \tau_f/\tau_e = 9\rho_f/(2\rho_p + \rho_f)$  is the ratio between the fluid time scale and the effective particle response

time. The function  $a_{\pm} = (-\sqrt{\beta} \pm (\beta - 4)^{1/2})/(2\sqrt{\tau_e})$  while the function  $E_{1/2}(a\sqrt{t}) = e^{a^2 t} \operatorname{erfc}(-a\sqrt{t})$ , denoting the Mittag-Leffler function of order  $\frac{1}{2}$ , which has been represented in terms of the complementary error function  $\operatorname{erfc}$ . In the long-time limit as  $t \rightarrow \infty$ , the MSD tends to Einstein's classical relationship of  $\langle X^2(t) \rangle = 2dDt$ .<sup>51</sup>

Similarly, the equation for the VACF as derived by Mainardi *et al.*<sup>22</sup> is

$$\frac{C_V(t)}{\langle V^2(0) \rangle} = \left\{ \frac{a_+ E_{1/2}(a_+\sqrt{t}) - a_- E_{1/2}(a_-\sqrt{t})}{a_+ - a_-} \right\}. \quad (31)$$

In this case,  $\langle V^2(0) \rangle$  is identical to the root mean square (RMS) velocity,  $V_{rms}$ , of the Brownian particle. The RMS velocity including the added-mass effect becomes  $\langle V^2(0) \rangle = dk_B T/m_e$ . In the long-time limit, Eq. (31) reduces to

$$\frac{C_V(t)}{\langle V^2(0) \rangle} = \sqrt{\frac{\beta}{4\pi}} \left( \frac{t}{\tau_e} \right)^{-3/2} \quad \text{as } t \rightarrow \infty. \quad (32)$$

Here, the well-established  $t^{-3/2}$  decay of the VACF predicted using molecular dynamics<sup>12</sup> is evident. The underlying explanation for this scaling is that the linear dimensions of the circulatory flow pattern that develops around the Brownian particle increase as  $(\nu t)^{1/2}$ , so that the velocity decays as  $(\nu t)^{-3/2}$  since total momentum is conserved.<sup>12</sup> Nevertheless, this form of the long-time scaling stems from the force model stated in Eq. (11). At finite  $Re_p$ , the long-time decay of the history force is considerably faster, as is today well established from simulations based on the full Navier-Stokes equations.<sup>52,53</sup>

For hindered diffusion scenarios, and when the wall is not too close ( $\tau_w \gg \tau_p, \tau_f$ ), the  $t^{-3/2}$  scaling may emerge on time scales shorter than  $\tau_w$ , after which the scaling transitions to<sup>54</sup>

$$\frac{C_{V,\parallel}(t)}{\langle V^2(0) \rangle} = \frac{3B}{2} \frac{\tau_w}{\tau_f} \left( \frac{t}{\tau_f} \right)^{-5/2}, \quad (33)$$

in the directions parallel to the wall, and

$$\frac{C_{V,\perp}(t)}{\langle V^2(0) \rangle} = \frac{3B}{2} \left[ A \left( \frac{t}{\tau_f} \right)^{-5/2} + \frac{\tau_w^2}{4\tau_f^2} \left( \frac{t}{\tau_f} \right)^{-7/2} \right], \quad (34)$$

in the wall-normal direction. From Eq. (34), it is seen that a  $t^{-7/2}$  scaling is expected to dominate for wall-parallel motion in the time window  $\tau_w \lesssim t \ll \tau_w^2/\tau_f$ , whereas at long enough times the  $t^{-5/2}$  scaling eventually prevails.<sup>54,55</sup> Here,  $B = (\rho_p/\rho_f + 1/2)/9\sqrt{\pi}$  and  $A = (2\rho_p/\rho_f - 5)/9$  are numerical constants that depend only on the particle-to-fluid density ratio. These behaviors of the parallel and perpendicular VACFs have been confirmed in molecular dynamics simulations<sup>56,57</sup> as well as experimentally,<sup>55</sup> although such experiments are extremely challenging due to the necessity to distinguish the color of the thermal noise from other experimental disturbances.<sup>8,55,57–60</sup>

The diffusivities for wall-adjacent diffusion in the long-time limit are<sup>39,58,61,62</sup>

$$D_{\parallel} = D_{\infty} \left( 1 - \frac{9r_p}{16h} + \frac{1r_p^3}{8h^3} - \frac{45r_p^4}{256h^4} - \frac{1r_p^5}{16h^5} \right), \quad (35)$$

and

$$D_{\perp} = D_{\infty} \frac{6h^2 - 10r_ph + 4r_p^2}{6h^2 - 3r_ph - r_p^2}, \quad (36)$$

where  $D_{\infty}$  is the unhindered diffusion coefficient and  $h$  is the distance of the particle center above the wall as previously mentioned. These expressions are valid in the limit  $\rho_p/\rho_f \rightarrow \infty$ .

The equation for the MSD derived from the CLE is<sup>63</sup>

$$\langle X^2(t) \rangle = 2dD \left( t - \frac{m_p}{\gamma} + \frac{m_p}{\gamma} e^{-t/\tau_p} \right) \approx 2dDt \quad \text{when } t \gg \tau_p. \quad (37)$$

This expression also reduces to the classical diffusion relation derived by Einstein at time scales much larger than  $\tau_p$ .<sup>51</sup> The VACF calculated from the CLE was given in Eq. (3). Whereas the CLE predicts an exponential decay of the VACF, the GLE, as well as molecular dynamics simulations, predicts a decay proportional to  $t^{-3/2}$  in the long-time range<sup>12,22,64</sup> and is sensitive to changes to the hydrodynamic environment brought about by other nearby surfaces. The emergence of the correct scaling in the long-time range is, therefore, a well-established way to assess whether the hydrodynamic description is adequate in the governing equations used.

## IV. RESULTS AND DISCUSSION

In this section, results will be presented and discussed first for the unhindered Brownian motion (Sec. IV A) and the wall-adjacent Brownian motion (Sec. IV B). The section will then conclude with an outlook on how the information provided in the memory kernel can be used to assess and monitor the state of a reactive particulate system (Sec. IV D).

### A. Unhindered cases

The purpose of the unhindered cases is primarily to validate the novel methodology developed in the current work against established

theoretical results. It will also be possible to illustrate the advantages of using a GLE-based approach over a CLE-based one. These goals are met by analyzing the MSD and the VACF predicted by the three methods explained in Sec. III F 1. Thereafter, we exploit the capability of the proposed methodology to derive the hydrodynamic memory kernel on-the-fly, to provide instantaneous characterizations of the spatio-temporal environment associated with the particle. Due to the symmetry of the case under study, all the results have been averaged over three directions.

### 1. MSD for unhindered motion

The MSD calculated from the unhindered Brownian motion simulations for different particle-fluid density ratios,  $\rho_p/\rho_f$ , using the three methods discussed (LPT using memory-kernel-based GLE, IB-FSI using memory-kernel-based GLE, and LPT using white-noise-based CLE) are compared against the theoretical expression derived from the GLE by Mainardi *et al.*<sup>22</sup> in Fig. 3. The classical Einstein diffusion expression  $\langle X^2(t) \rangle = 2dDt$  is also drawn in these figures to illustrate how the Brownian particle behavior tends toward the long-term diffusive behavior at different particle-fluid density ratios. For short times, the Einstein expression is not valid, as an immersed particle undergoes a ballistic motion with  $t^2$ -scaling in the MSD.<sup>22,32</sup> This ballistic regime is also clearly visible in our simulation results.

In Fig. 3, the results for the MSD are normalized by dividing with  $D\tau_p$  to get non-dimensionalized graphs. The memory-kernel-based GLE simulations can be seen to produce MSD results that are in very good agreement with the theoretical prediction provided by Mainardi *et al.*<sup>22</sup> across all particle-to-fluid density ratios investigated, irrespective of whether the hydrodynamic force on the particle is determined using the LPT framework or the IB-FSI framework. The CLE-based simulations, however, underpredict the diffusion undergone by the particle at the lower density ratios, as expected. The deterioration of the CLE-based approach is particularly pronounced at density ratios 1 and 10, and it is attributed to the white-noise formulation of the Brownian force in the CLE simulations, which underpredicts the magnitude of the Brownian force, as it does not account for the added mass and history effects. The diffusive behavior of the particle tends toward the classical trend predicted by Einstein in the long-time regime. However, the time taken to approach this behavior increases as the added mass and history effects become more dominant at the lower density ratios, in agreement with theory.<sup>22,57</sup> At high density ratios, such as 100 and 1000, the MSD lines from all three methods clump together and overlap well with the theoretical lines. This also confirms the theoretical understanding that the added mass and history effects become negligibly small at high particle-to-fluid density ratios. The hydrodynamic force can, under such circumstances, be modeled as purely drag-based and the differences in the diffusive behavior of the particle would be negligible at such high density ratios.

In conclusion, the MSD results show that the GLE-based IB-FSI approach developed in the current work is indeed able to correctly describe Brownian diffusion with significant hydrodynamic memory effects.

### 2. VACF for unhindered motion

The VACF graphs are normalized by dividing them with the RMS velocities at each density ratio (calculated using the effective mass

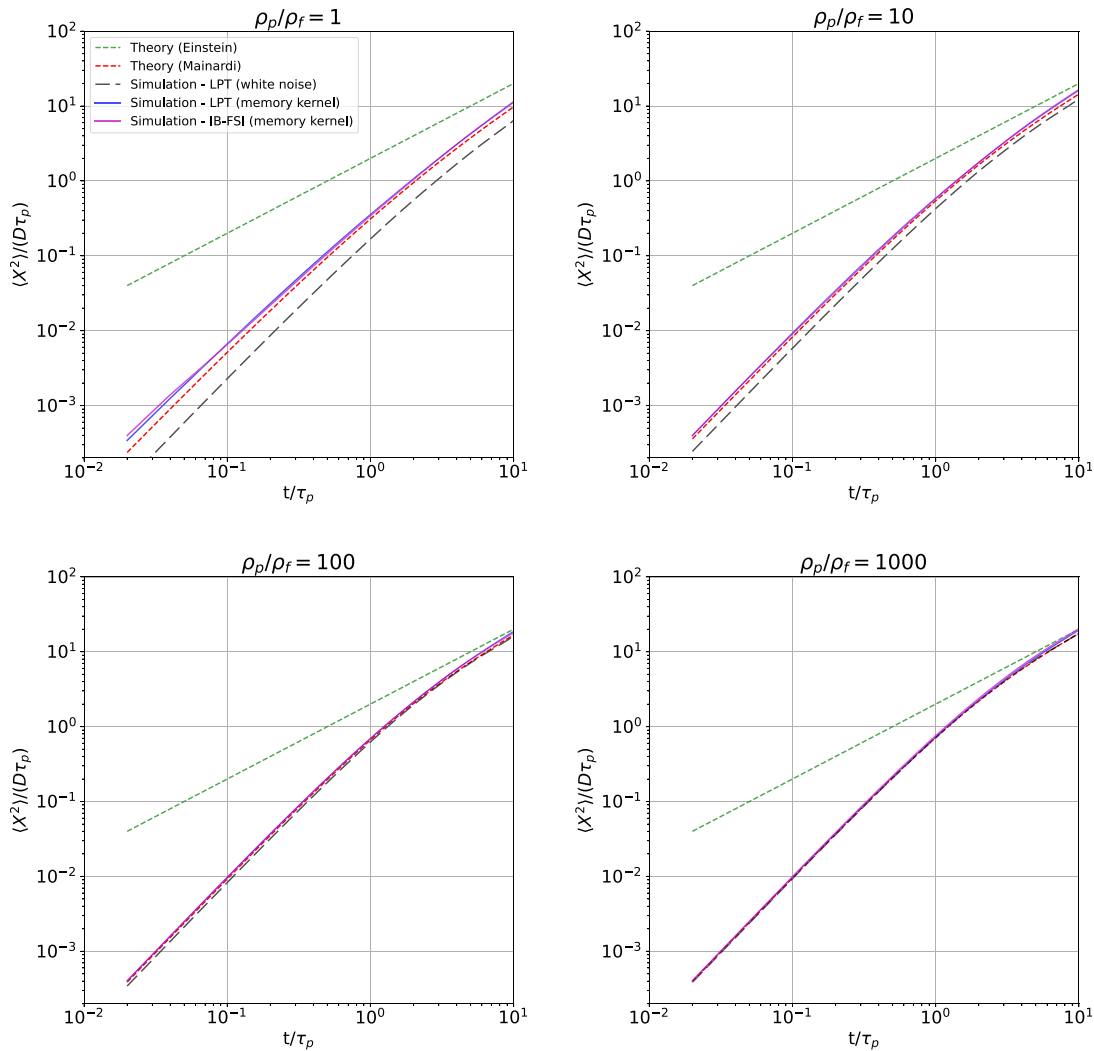


FIG. 3. Mean square displacement (MSD) of a Brownian particle in unhindered diffusion at different density ratios.

of the particle), giving the results shown in Fig. 4. The GLE-based simulations in this case also provide results that are in agreement with the theoretical predictions from Mainardi *et al.*<sup>22</sup> The oscillations in the VACF graph toward the long time-lag region ( $t/\tau_p > 1$ ) can be attributed to the low number of sampling points at large time separations. At the lower particle-fluid density ratios (1 and 10), the VACF trend from the GLE simulations are significantly closer to the theoretical estimates than the CLE simulations. The latter underpredict the root mean square velocity, as seen from the much lower starting points of the VACF curves.

The VACF graph from the GLE simulations at density ratio 1 shows fluctuations at short time scales, which can be attributed to the choice of time step size (if the time step size is decreased further, below the time regime of interest for the VACF calculations, these oscillations shift toward even lower time scales). Similar to the behavior in the MSD graphs, at the higher density ratios of 100 and 1000, the VACF

graphs clump closer together with the GLE and CLE simulations overlapping with the theoretical predictions from Mainardi *et al.*<sup>22</sup> as well as the decay rate expected from classical Langevin theory shown in Eq. (3). At lower density ratios, the VACF can be seen to be proportional to  $t^{-3/2}$  as it follows the theoretically expected behavior;<sup>22</sup> the velocity of the particle remains correlated for longer time periods due to the strong history effect. However, at higher density ratios the velocity decorrelates much more quickly, tending close to the exponential decay predicted from the CLE. It should be noted here that improved CLE-based approaches, where the white noise is modified on-the-fly based on the thermal energy of the particle, allows for a closer match to the theoretically expected MSD and VACF curves.<sup>21</sup>

The good agreement between the current simulation results and the available theoretical predictions further underlines the capabilities of the developed methodology to accurately characterize Brownian motion on time scales  $\mathcal{O}(\tau_p)$  in a continuum framework.

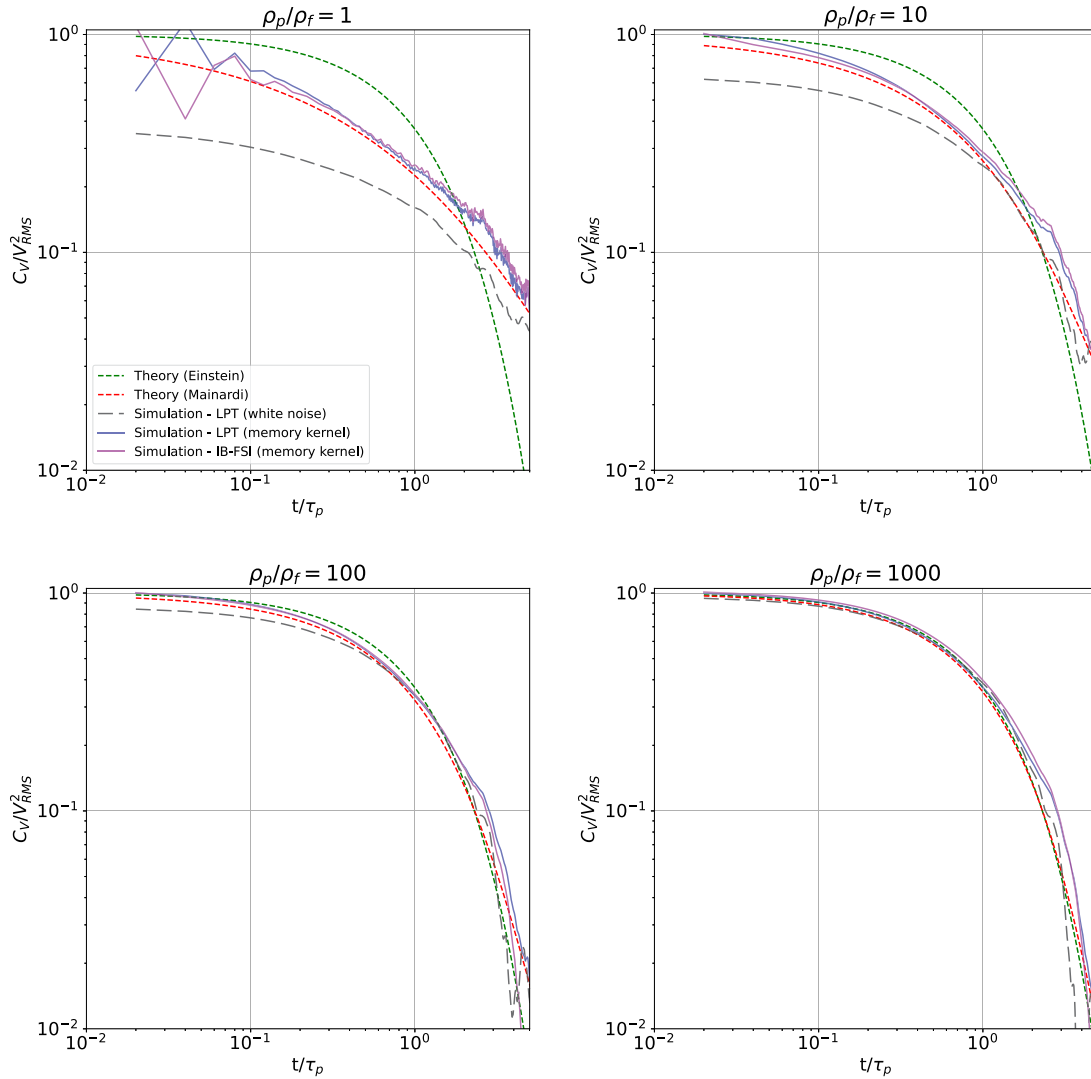


FIG. 4. Velocity auto-correlation function (VACF) of a Brownian particle in unhindered diffusion at different density ratios.

### 3. Memory kernels for unhindered motion

The memory kernel estimated from the simulations is a continuum representation of molecular phenomena that creates the drag, added mass and history effects. The kernel contains information about all these three effects lumped together. Furthermore, the kernel also contains a description of how this information has evolved with time, such that the dependence of the current hydrodynamic force on the velocity history is accounted for. Graphical representations of the memory kernels obtained from the LPT and IB-FSI frameworks are shown in Fig. 5.

The first term in the theoretical memory kernel [Eq. (7)] derived by Dufty<sup>24</sup> involves the term  $2\gamma\delta(\tau)$ , which represents the initial peak in the memory kernel that results from the instantaneous drag effect on the particle. The kernels obtained from the simulations have, thus,

been normalized using  $2\gamma/\Delta\tau$ , which is the numerical representation of the same term (here, the  $\delta(\tau)$ -function is represented as  $1/\Delta\tau$ , where  $\Delta\tau$  is the time step of the simulation). The normalized memory kernels ( $K^*$ ) for the unhindered simulations, from the LPT and IB-FSI frameworks, and at different density ratios, are shown in Fig. 5. The memory kernel values are relatively constant throughout the simulation, since the changes in the particle position relative to the domain are quite small. In order to depict the general hydrodynamic kernel, the memory kernels have also been averaged over all the simulation timesteps and then plotted in Fig. 5. Thus, the memory kernels dependency on the instantaneous time  $t$  through its position has been removed here and the kernel value shown in Fig. 5 depends only on the lag time  $\tau$  [i.e.,  $K^*(t, \tau) = K^*(\tau)$ ]. The kernel tails (when  $\tau/\tau_p > 1$ ) show oscillations (that are less than  $10^{-5}$  after normalization). These tail value oscillations can be attributed to the attempts

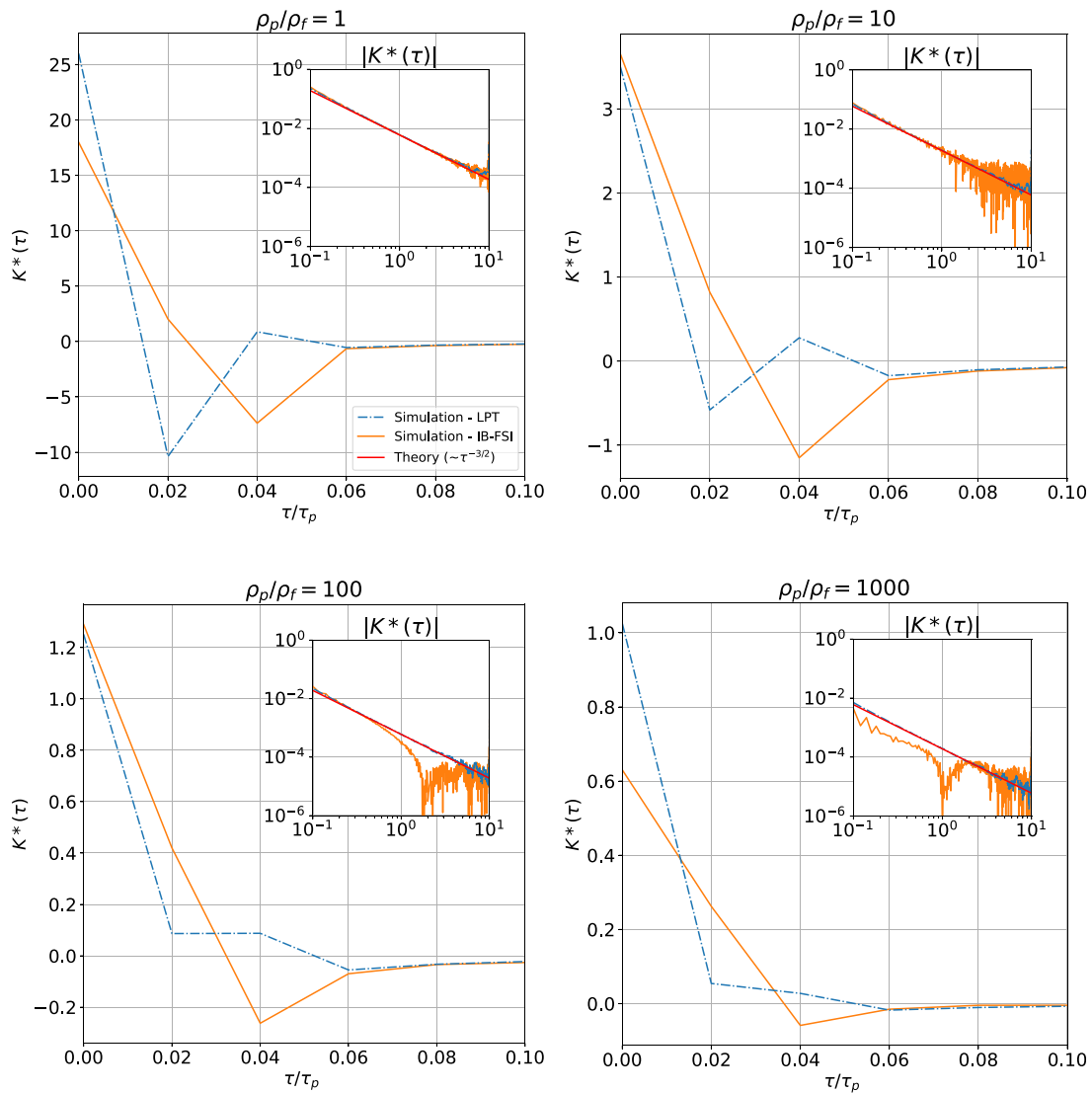


FIG. 5. Memory kernel of a Brownian particle in unhindered diffusion at different density ratios.

made by optimization procedure to reduce the cost function by varying the tail end of the kernel at every time step to get it as close to the hydrodynamic force as possible. The shape of the kernel in the initial part up to a time lag of  $5\Delta\tau = 0.1\tau/\tau_p$  is represented linearly with respect to time, while the remaining portion is represented logarithmically with respect to time as an inset in the same figure. The theoretical memory kernel from Eq. (7) is also drawn in the logarithmic inset to compare the kernel developed using the optimization procedure to the corresponding theoretical value. The LPT and IB-FSI kernels have different values, especially at short time separations, due to the different procedures used to determine the hydrodynamic force on the kernel as well as differences in the time discretization. The overall behavior, with a peak at 0 time separation, a negative dip thereafter, and a  $\tau^{-3/2}$  slope at long time separations, is, however, the same for both methods.

The kernels, thus, have an initial spike at  $\tau = 0$  as expected from the theoretical representation involving the  $\delta(\tau)$ -function. However, it can be seen that the value of the spike decreases as the particle-to-fluid density ratio increases from 1 to 1000. At the highest density ratio of 1000, the peak is the lowest and quite close to 1 from both the frameworks. The peak in the memory kernel at  $\tau = 0$  can be seen to increase as the density ratio is reduced. This rise can be attributed to the increasing contributions to the kernel from the added mass effect, which become more prominent as the particle-to-fluid density ratio reduces. The theoretical expression in Eq. (7) was derived by excluding the added mass effect. The numerical (discretized) value of the memory kernel comprises the series of coefficients that the velocity history of the particle needs to be multiplied with (along with the time step) to add up to the hydrodynamic force it experiences, as shown in the cost

function [Eq. (14)]. From this understanding of the terms of the memory kernel, if the added mass effect were to be included into the memory kernel as shown in the second term on the right side of Eq. (11), then the initial spike in the kernel would instead be produced by  $2[\gamma + (m_p \rho_f)/(2\rho_p \Delta\tau)]/\Delta\tau$ , which proportionally increases as the particle-to-fluid density ratio reduces. The initial peaks of the memory kernels obtained for the unhindered case and normalized in this way are shown in Fig. 6. They are compared against the theoretical peaks mentioned previously that include the drag and the added mass effect. The proportional increase in the kernel peaks can be seen from the fitted kernels that have been estimated as part of the unhindered Brownian motion simulations using both frameworks. The memory kernel peak from the LPT simulation can be seen to overlap very well with the theoretical prediction for the peak. This makes sense, since the force in the LPT framework and the theoretical peak were both developed from Eq. (11). The peaks from the IB-FSI framework do not exactly follow the same trend but still show the expected decrease as the particle-to-fluid density ratio increases. Possible reasons for this variation include the difference in the method used to determine the force on the particle as well as the different time stepping scheme used in the IB-FSI framework.

The added mass effect is proportional to the acceleration of the particle, as shown in Eq. (11), which numerically depends on the difference between the velocities of the particle at time steps  $t$  and  $t - \Delta t$ , as shown in the discretized version [Eq. (24)]. The added mass effect, thus, consists of a positive contribution proportional to the current velocity of the particle and a negative contribution that is proportional to velocities in the past, where the exact characteristics depend on the force model and time advancement algorithm used in the simulation framework. The dip in the kernels at small but finite time, especially prominent at lower particle-to-fluid density ratios, is due to this negative contribution to the kernel from the added mass

effect. There are also influences on the kernel values from the history effect. In the memory kernel obtained from the LPT framework, the history effect creates a positive contribution which reduces the dip in the second value of the kernel, taking it above zero at higher density ratio. The LPT-based memory kernel can also be seen to have a second spike that is due to this positive contribution from the history force model used in these simulations. In the IB-FSI framework, higher-order time stepping is used causing the drag, the added mass and history effects to become spread out over more time steps, leading to the dip in the kernel being shifted further in time from the initial peak.

The tails of the memory kernels from both the frameworks shown in the logarithmic insets can also be seen to closely follow the theoretical scaling [shown in Eq. (7)], with a  $\tau^{-3/2}$  trend as expected. The strength of the tail of the memory kernel created by the history effect is proportional to the viscous fluid time scale  $\tau_f$ . This time scale becomes much smaller than the particle response time (used to determine the simulation time step) at higher density ratios, and consequently, the contribution to the memory kernel from the history effect reduces. The magnitude of the tail of the kernel, thus, becomes quite small at the higher density ratios, as seen from the kernels obtained from the simulations as well as the theoretical values shown in Fig. 5. As the particle-to-fluid density ratio goes to infinity, the kernel, thus, tends toward  $2\gamma\delta(\tau)$ , which is the expected value for a pure white-noise Brownian motion involving only steady drag effects. In this way, the memory kernel carries indirect information about the effective viscosity of the surrounding fluid, which could potentially be exploited by using Brownian particles to probe complicated geometries in complex fluids.

The memory kernel is also a representation of how the Brownian forces are correlated in time, as stated mathematically in Eq. (10). Thus, the initial peak in the memory kernel indicates the variance of the force. The subsequent terms represent how the *current* Brownian force correlates with the *past* forces. The decay in the kernel is the rate at which the force covariances decay over time. In the GLE-based method, the memory kernel is used to generate the covariance matrix for the Brownian force based on this understanding (cf. Sec. III C). The covariance matrix is factorized into two root matrices which are then multiplied with normally distributed random numbers to generate the random Brownian force. Since the root matrix of the covariance matrix is influenced by the values of the memory kernel, the final Brownian force generated contains contributions proportional to the values of the memory kernel. In conclusion, the peak of the memory kernel represents the immediate influence, while the remaining terms add contributions from the past.

As the added mass effect becomes more pronounced at low density ratios, the temporal discretization of the particle behavior starts to have an influence on the behavior of the VACF curve, as previously noted (cf. Fig. 4). This effect was further investigated in a time step study, where it was confirmed that the fluctuations shift toward even shorter time scales as the time step is reduced, as shown in Fig. 7(a). Furthermore, removing the explicit added mass contribution [the second term on the right-hand side of Eq. (24)], and instead accounting for the added mass effect via modifying the particle mass [ $m_{p,mod} = m_p(1 + \rho_f/(2\rho_p))$ ], makes the fluctuations disappear completely. Moreover, as shown in Fig. 7(b), the normalized memory kernel and Brownian force correlations are in very good agreement for

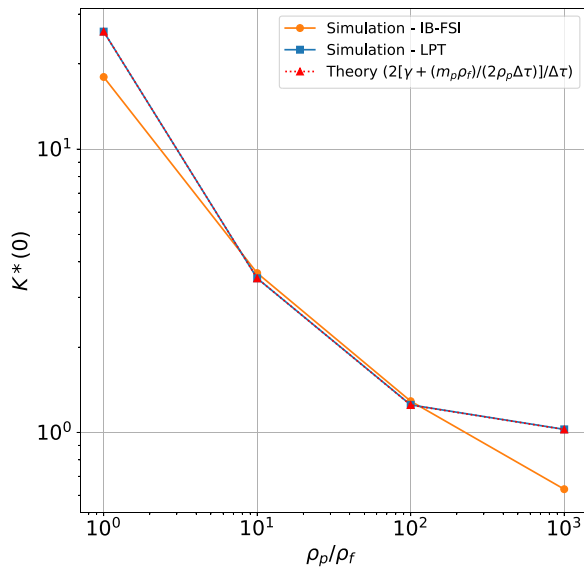
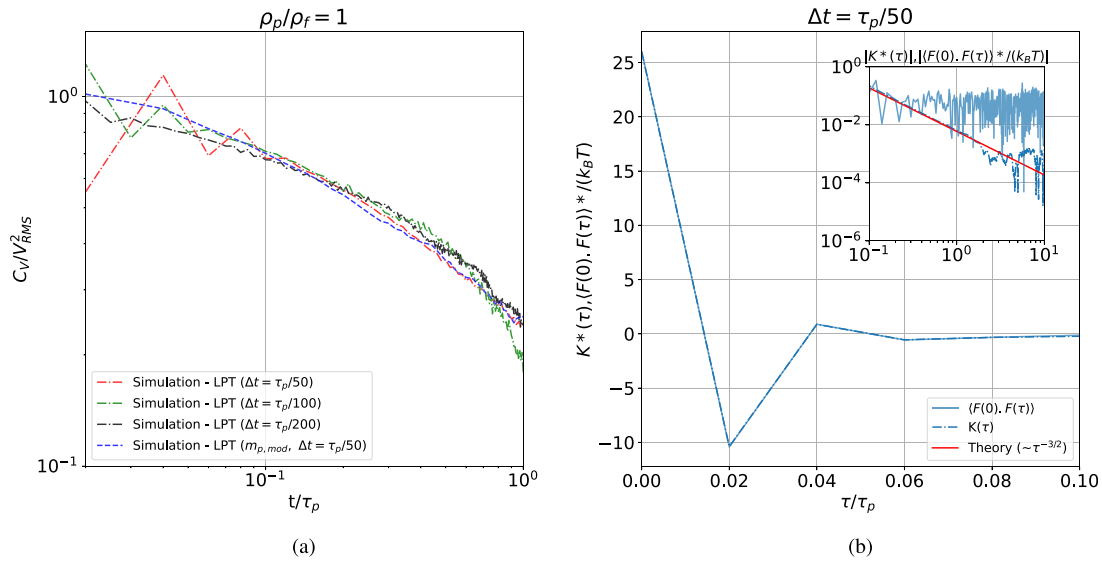


FIG. 6. The normalized initial peaks of the memory kernel as obtained in the unhindered scenario from the LPT and IB-FSI frameworks at particle-to-fluid density ratios from 1 to 1000. The theoretical peaks  $(2[\gamma + (m_p \rho_f)/(2\rho_p \Delta\tau)]/\Delta\tau)$  are also included for comparison.



**FIG. 7.** (a) Velocity auto-correlation function (VACF) of a Brownian particle in unimpeded diffusion at density ratio 1 for different time step sizes ( $\tau_p/\Delta t = [50, 100, 200]$ ). Also plotted is the same VACF when the particle acceleration is calculated using the modified mass [ $m_{p,mod} = m_p(1 + \rho_f/(2\rho_p))$ ] without an explicit added mass force. (b) The normalized memory kernel and the normalized Brownian force correlations used in the simulation with a time step of  $\Delta t = \tau_p/50$ . The results depict how the fluctuation–dissipation relation between the Brownian force and memory kernel is maintained in the simulation.

short time separations already in the  $\Delta t = \tau_p/50$  case, highlighting the consistency of the implemented methodology. Taken together, these observations confirm that the fluctuations seen in the VACF at short time scales for low density ratios are related to the numerical representation of the added mass effect, and that they do not compromise the accuracy of the colored force generation.

Although the memory kernels generated by the LPT and IB-FSI framework differ, especially in the beginning portion of the kernel, the MSDs and VACFs generated using both frameworks match well with the theoretical results, as previously shown in Figs. 3 and 4. Thus, the memory kernel estimates can be concluded to be valid continuum approximations of molecular phenomena that are represented using the GLE.

## B. Wall-adjacent cases

The wall-adjacent cases offer the possibility of evaluating the novel methodology developed in the current work against experimental and theoretical results for Brownian motion close to solid surfaces. Here, we analyze the MSD and the VACF predicted by the IB-FSI method for the wall-adjacent configuration (cf. Sec. III F 2). In particular, we wish to assess whether the proposed methodology is able to accurately produce the expected particle statistics, in which the effect of the presence of the solid boundary is not only evident in all three coordinate directions but also significantly different in the wall-normal and wall-parallel directions. Finally, we again exploit the capability of the developed methodology to derive the hydrodynamic memory kernel on-the-fly, to provide instantaneous characterizations of the spatio-temporal environment associated with the particle, to reveal how this is changing with the presence of a nearby solid boundary. Due to the symmetry in the two directions parallel to the wall, the results over these two directions have been averaged.

## 1. MSD for wall-adjacent motion

In the wall-adjacent case, the diffusive behavior of the Brownian particle varies depending on whether the particle is moving parallel to or perpendicular to the direction of the wall. In both cases, the MSD of the particle reduces since the hydrodynamic resistance to the motion increases.<sup>4,65</sup>

As shown in Fig. 8, the MSD from the GLE-based simulations at density ratios  $\rho_p/\rho_f = 1$  and 10 exhibit the expected decrease in diffusion due to the increased hydrodynamic resistance. The decrease is more significant in the wall-normal direction as compared to the wall-parallel directions. Thus, in addition to a period of anomalous diffusion, where the MSD requires more time to approach the long-time diffusive behavior, the Brownian diffusivity established at long enough time will also be lower than the Einsteinian diffusivity of the unimpeded setting. All of these trends are visible in the numerical results and corroborate well with theoretical expectations.

At  $\rho_p/\rho_f = 1.96$ , Jeney *et al.*<sup>55</sup> measured the reduction in the diffusion coefficient at a separation of  $y = 2.2r_p$  and found it to agree with the theoretical predictions in the long-time limit. We, therefore, evaluate the reduction of the long-time diffusion due to the presence of a wall at  $h = 1.25r_p$  from Eqs. (35) and (36). By doing so, we may establish that at  $t/\tau_p = 10$ , the wall-parallel MSD is within 0.2% of its long-time limit for  $\rho_p/\rho_f = 10$ , and within 20% for  $\rho_p/\rho_f = 1$ . These observations, thus, suggest that the wall-adjacent MSDs are in excellent agreement with the theoretical expectations, as the time needed to reach the terminal diffusivity increases as the density ratio decreases. For the wall-normal direction, the expression in Eq. (35) is an approximation obtained by a regression of an infinite series,<sup>62</sup> and it is expected to be less accurate at small separations. Our wall-normal MSDs are within 7%–30% of the long-time limits expected using this approximate expression. In conclusion, the wall-adjacent MSDs are

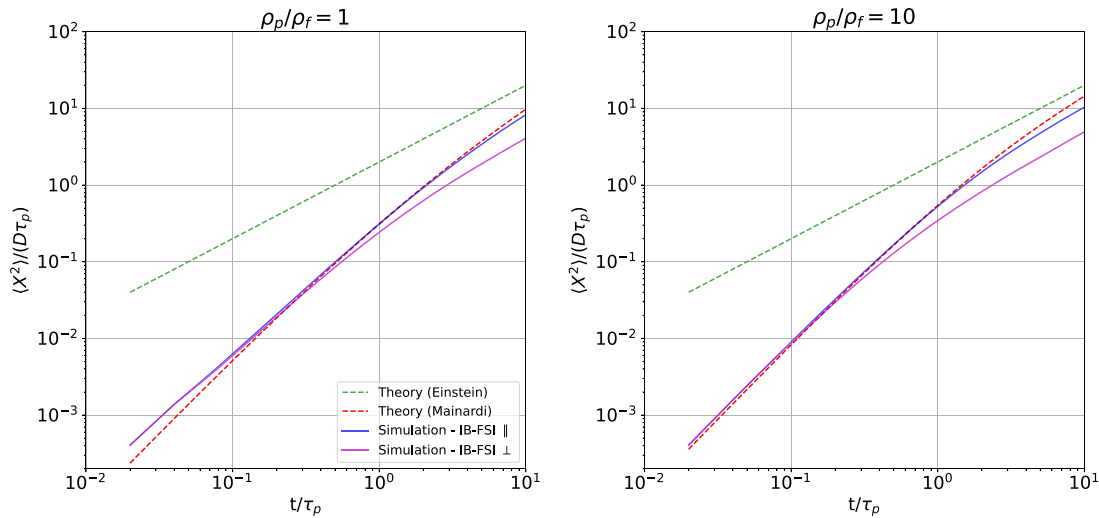


FIG. 8. Mean square displacement (MSD) of a Brownian particle diffusing close to a solid wall at two different density ratios.

considered to be in very good agreement with the available theoretical predictions.

**2. VACF for wall-adjacent motion**

The particle velocity de-correlates quicker in the presence of nearby solid boundaries, as the boundary limits the development of the induced flow structures surrounding the particle. Consequently, the VACF decays faster close to a wall, with the effect being significantly different in the wall-normal and wall-parallel directions.<sup>54</sup> Figure 9 displays the VACFs obtained from the current IB-FSI simulations, separated into wall-normal and wall-parallel components. Also indicated in these graphs are the theoretically predicted decays of  $t^{-7/2}$  in the normal direction for intermediate times, and  $t^{-5/2}$  which is the

decay expected in the parallel directions<sup>54</sup> and in the normal direction at long times. The upper time limit of the VACF graphs is extended to  $t/\tau_p = 10$  to better see the decay trends, especially at the lower density ratio.

It should be noted here that the particle is relatively close to the wall, such that  $\tau_w > \tau_f > \tau_p$ , whereas  $\tau_w \gg \tau_f, \tau_p$  is not fulfilled. The time scale relations are, thus, similar to those studied experimentally by Jeney *et al.*,<sup>55</sup> where the shortest particle-surface separation was characterized by  $\tau_f = 2.25\tau_p$  and  $\tau_w = 23\tau_p$ . In our simulations, at  $\rho_p/\rho_f = 1$ ,  $\tau_f = 4.5\tau_p$  and  $\tau_w \approx 7\tau_p$ , whereas at  $\rho_p/\rho_f = 10$ ,  $\tau_f = 0.45\tau_p$  and  $\tau_w \approx 0.7\tau_p$ . Therefore, one may expect the  $t^{-5/2}$  slope in the wall-parallel VACF statistics to be clearly visible in our data for  $\rho_p/\rho_f = 10$ , whereas for  $\rho_p/\rho_f = 1$  it may be obscured by noise. This prediction is in perfect agreement with the simulation results: a clear

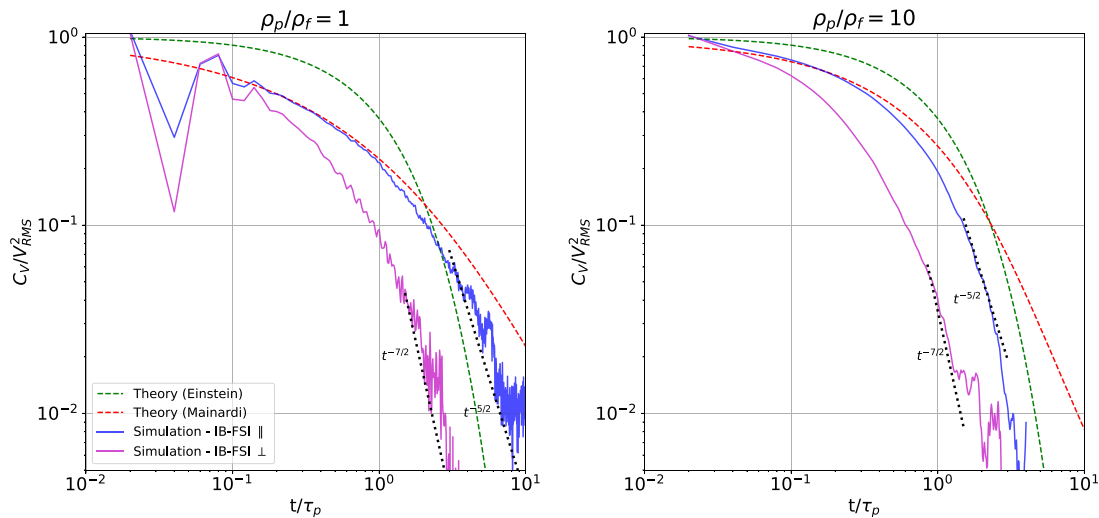


FIG. 9. Velocity auto-correlation function (VACF) of a Brownian particle diffusing close to a solid wall at two different density ratios. Trendlines for the  $t^{-5/2}$  and  $t^{-7/2}$  scalings are included to guide the eye.

$t^{-5/2}$  slope emerges in the parallel VACF at the higher density ratio. At the same time, the earlier de-correlation (as compared to the  $t^{-3/2}$  scaling) is clearly visible for the lower density ratio, while the slope approaches  $t^{-5/2}$  around  $t/\tau_p \approx 5$  (although this part of the graph is indeed somewhat noisy).

Similarly, the intermediate  $t^{-7/2}$  slope in the wall-normal VACF statistics expected beyond  $t/\tau_p \approx 0.7$  when  $\rho_p/\rho_f = 10$  is also clearly visible in our simulation results. This scaling can also be discerned for the lower density ratio, as the normal and parallel VACF lines separate much earlier than at  $t = \tau_w$ . The anisotropy introduced by the wall is very pronounced for both density ratios investigated. All of these observations are in good agreement with the experimental observations of Jeneý *et al.*,<sup>55</sup> which are also supported by theoretical predictions.<sup>40,54</sup> It is, thus, concluded that the proposed method is indeed capable of correctly predicting colored Brownian motion in wall-adjacent configurations.

### 3. Memory kernels for wall-adjacent motion

The memory kernels for the wall-adjacent configuration obtained from the IB-FSI framework as a part of the developed methodology are shown in Fig. 10. The memory kernels have been averaged over the simulation duration as described previously in the unhindered scenario to obtain their general form. When contrasted against the two top panels in Fig. 5, which show the corresponding results obtained for unhindered diffusion, it is evident that the peak of the memory kernel has shifted up. This shift indicates an increase in the drag and added mass effects close to the wall, which is more pronounced in the wall-normal direction as expected from theory.<sup>4,40</sup> Furthermore, the tails change slope at long times (as seen from the insets of Fig. 10), and at the same time, the scaling for the wall-normal and wall-parallel memory kernels starts to differ, indicating the direct relation between the kernel and the VACF. In conclusion, the variation in the memory kernel matches the shifts in the MSDs and VACFs, which proves that the method is capable of capturing domain changes at low density ratios.

The circulatory flow pattern around the particle responsible for the history effects and the emergence of the  $t^{-3/2}$  scaling in the VACF in the unbounded case, and the  $t^{-5/2}$  and  $t^{-7/2}$  scalings for the same in the wall-adjacent configuration, are depicted in Fig. 11. It is clearly seen that the unhindered configuration permits the evolution of a symmetric vortex flow pattern, in agreement with molecular dynamics investigations.<sup>12</sup> It is also evident that the presence of a nearby solid surface imposes a geometrical restriction on the evolution of the flow structures in the vicinity of the particle, which significantly changes its hydrodynamic environment.

### C. Notes on computational cost and scalability

It takes approximately 50–100  $\tau_p$  for the peaks and valleys of the memory kernel to fully stabilize to their equilibrium value at a given position in the optimization procedure employed. Once a complete memory kernel has been developed, the continued process is very efficient. These numbers imply that the memory kernel itself, which contains all information needed to eventually produce the correct statistical behavior in the integration of the particle equation of motion, can be well established in a much shorter time frame than what is needed for the statistics (i.e., MSD and VACF) to converge. This observation opens up for possible computational optimizations of the methodology, wherein the frequency of memory kernel updates may potentially be relaxed once initial stabilization has been confirmed. Alternatively, memory kernel updates could be triggered only for particles whose local configuration has changed beyond some threshold. It is also possible to imagine an LPT-based methodology applicable to geometrically complex situations, where the total hydrodynamic force and the colored Brownian force are both determined from memory kernels obtained on-demand using a multiphase DNS framework such as the IB-FSI method employed here. In such a hybrid framework, DNS-quality force covariances and magnitudes could be sampled using the IB-FSI method, while the long term-statistics are produced using a computationally less expensive LPT-based method.

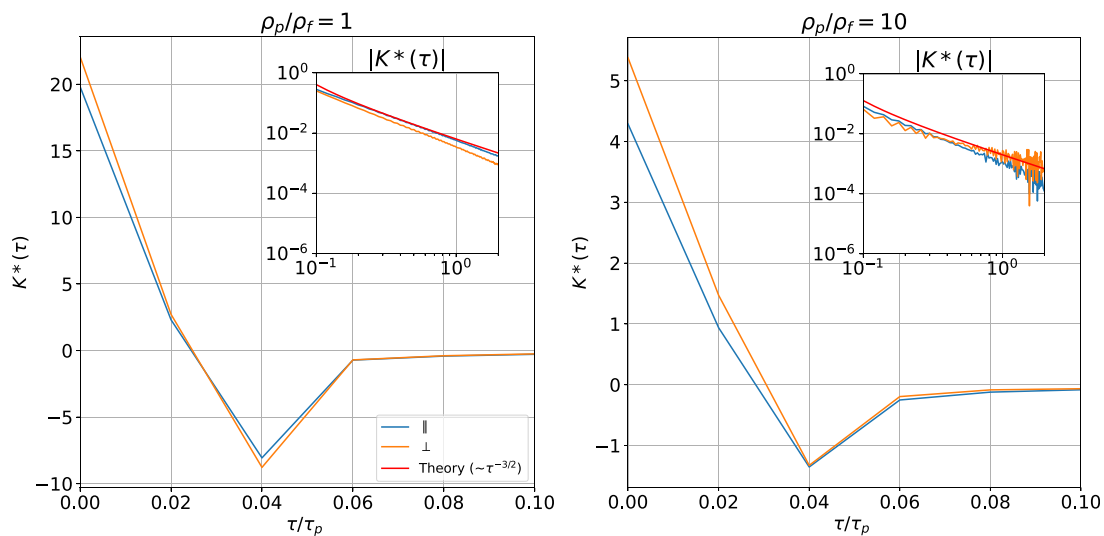
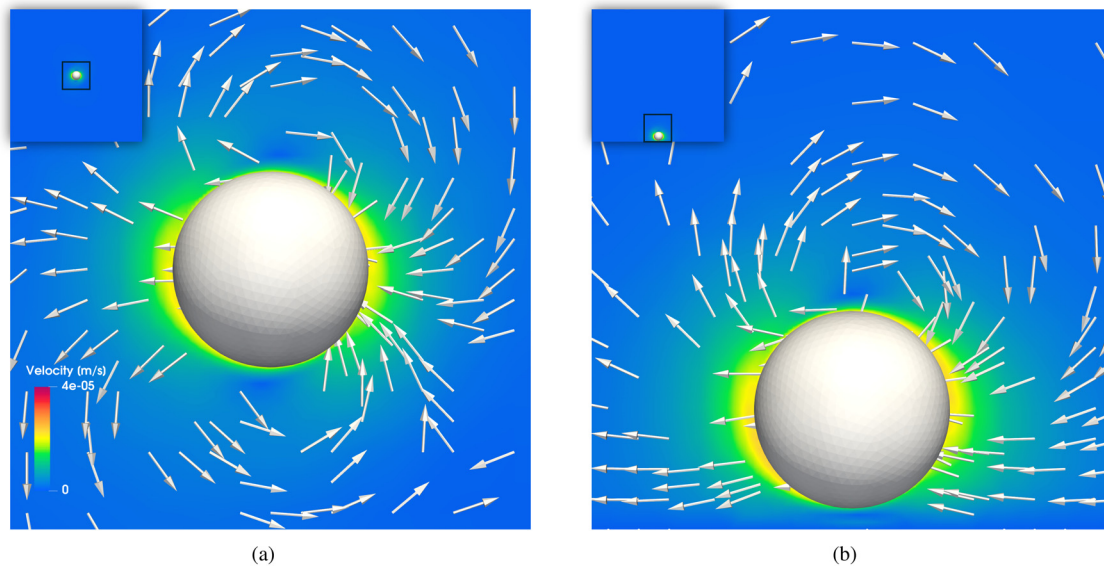


FIG. 10. Memory kernel of a Brownian particle diffusing close to a solid wall at two different density ratios.



**FIG. 11.** The velocity field surrounding the particle at the same sample time instance is portrayed for the unimpeded and wall-adjacent cases in (a) and (b), respectively. The velocity has been projected onto the  $yz$ -plane. On the top-left corner of the panels (a) and (b), a slice of the simulation domain that passes through the center of the particle is shown as insets. The black box in the inset indicates the area around the particle that is shown in the enlarged figures. These figures also show the velocity plotted as unscaled vectors to indicate the flow direction. The magnitude of the velocity is given by the contour plot with its scaling indicated in the lower left corner of panel (a).

The current framework has not yet been fully optimized with regard to computational performance. For example, the current methodology for the colored force generation relies purely on the temporal covariance between the Brownian forces as described by the memory kernel. There are alternative approaches using discrete Fourier transforms into the frequency domain that can be used instead, which could potentially yield additional speed-up.<sup>26,27,66</sup> In particular, it would be interesting to investigate whether the method proposed by Jung *et al.*<sup>67</sup> could be leveraged to ensure positive-semidefiniteness of the covariance matrix (by neglecting imaginary contributions), thereby avoiding constrained optimization, which should also increase the computational efficiency of the overall framework.

Extension of the methodology to a multiparticle system is relatively straightforward, as the whole particle system can be simulated with the multiphase DNS approach to determine the hydrodynamic force on each particle. The memory kernel, which carries the spatiotemporal correlations applicable for each particle can then be determined using the optimization routine specified in this work, allowing for the simulation of Brownian motion applicable to the local configuration of each particle. As the particle or domain geometry becomes more complicated than the symmetric scenarios explored in this work, the off diagonal terms of the memory kernel could potentially become significant. Future extensions to the methodology could explore optimization routines to estimate these terms as well from the hydrodynamic force and velocity history of the particle. The method could also be extended to include the rotational Brownian dynamics of the particle by including the memory kernel terms associated with rotational motion,<sup>25</sup> which would require the determination of the hydrodynamic torque acting on the particle and the associated angular velocity history of the particle.

A noticeable advantage of the proposed methodology is that all hydrodynamic interactions between particles are accounted for via the

continuum fields of the continuous phase; hence, the computational cost associated with obtaining  $\mathbf{F}_H$  is essentially independent of the number of particles in the system (in practice a higher number of particles may require more computational cells for adequate resolution of the continuum fields, thereby introducing a weak scaling with the number of particles). As these interactions are taken care of intrinsically, there is consequently no costly looping over particle pairs, introduction of arbitrary cutoff distances for particle-particle interactions, or neglect of multiparticle interactions. Complex geometries are easily handled within the IB-FSI framework, which alleviates the need to generate body-conforming meshes. The methodology is, thus, well suited for investigations of Brownian systems of considerable geometric complexity. The determination of the memory kernel for each particle (needed for the calculation of  $\mathbf{F}_B$ ) introduces a more direct scaling of the computational cost with the number of particles in the system. For simulations of extended duration, the computational performance could be further improved by decreasing the frequency at which the memory kernels are updated. For example, instead of re-optimizing every memory kernel for every particle in every time step, one could devise a scheme in which the memory kernels are only updated whenever the spatial configuration has changed beyond some threshold value since the last update. Within such a scheme, it would also be possible to divide the particle system into subsets, so that memory kernels updated would only occur for particles within a section of the complete geometry where the configuration is deemed to have changed significantly.

#### D. Outlook on future possibilities

The memory kernel constitutes a rich spatiotemporal characterization of the combined effect of the hydrodynamic environment surrounding the particle and the particle's response to it. There are many

natural and industrial particulate flow systems in which knowledge about particle reactivity is extremely valuable for optimization of design and operation. Unfortunately, it is typically difficult to measure particle reactivity *in situ* in a reliable and non-intrusive manner. It can, therefore, sometimes be easier to observe or characterize how particles move in the system. If a meaningful correlation can be established between particle reactivity and particle mobility, significant advances may unravel with regard to design and control strategies. The hydrodynamic memory kernel, thus, constitutes a perfect option for the establishment of a “fingerprint” to link mobility to reactivity.

As an example, for combustion-generated nanoparticles, a link between particle mobility and particle reactivity has previously been established theoretically and verified experimentally.<sup>68</sup> If particle mobility is characterized via deposition experiments under controlled conditions, the difference between the observed particle behavior and the theoretically expected behavior of an inert particle forms the basis for optimizing the parameters of a conceptual model.<sup>69</sup> In this case, the conceptual model, thus, provides the “fingerprint” of the expected particle reactivity.

The aforementioned example is but one out of many possibilities to correlate mobility to reactivity for small particles. Changes to the effective shape or size of a particle may also be inferred from the memory kernel components, as such changes will affect the hydrodynamic response to the particle, and the rate at which this response evolves over time will impact the instantaneous memory kernel via the hydrodynamic memory effect. This situation means that the memory kernel can be used to monitor processes involving particle agglomeration, heterogeneous reactions, and phase change phenomena. Effectively, the memory kernel, thus, constitutes a “fingerprint” that correlates with reactivity whenever reactions change the particle or its surroundings, and that provides an instantaneous characterization of the reaction environment of individual particles in complex, dynamic assemblies. The possible implications of fully exploiting this research direction are significant: The characterization of mechanical forces exerted on cancer cells may serve as an indicator of a tumor’s malignancy state.<sup>70</sup> The behavior of a Brownian particle close to a surface constitutes a “noise fingerprint,” the interpretation of which can form a basis for extending the functionality of surface-based sensing techniques for analytes in mixtures.<sup>71</sup> The concentration gradients of molecular solutes can move solid particles at fluid-membrane interfaces, leading to colloid accumulation or depletion, potentially playing a crucial role in degradation of interfacial contaminants<sup>72</sup> or at the emergence of chemiosmosis and the origin of life itself.<sup>73–75</sup> Future exploitation of, and investigation into, these and related applications depend on the availability of highly accurate methods for producing memory kernel information valid for complex systems.

On a related note, viscoelastic fluids may also exhibit memory effects that are different from their viscous fluid counterparts.<sup>33,76</sup> The study of many biological fluids, including blood and mucus, require such viscoelastic modeling of the fluid while also incorporating the Brownian motion of particles suspended in the media.<sup>76</sup> The capability to simulate transient viscoelastic fluid flow has already been implemented in the IB-FSI framework,<sup>77</sup> allowing for investigations of Brownian motion in viscoelastic environments using the proposed methodology. The memory kernels generated in such simulations could then serve as “fingerprints” of the local viscoelasticity sampled by a particle, which allows for an alternative characterization of the

viscoelasticity of the fluid under study relevant to important biological processes.

The developed framework herein can extract memory kernels for situations that are difficult or even impossible to arrange experimentally. Therefore, the proposed methodology is not only a tool for high-fidelity simulations of colored Brownian motion in systems of arbitrary geometric complexity, but also a tool for data generation to assist in the interpretation of experiments and for increased understanding of complex multi-physics systems where Brownian motion plays a key role. In the ongoing development of large-scale data-driven approaches to modeling and optimization of complex systems, we anticipate that the proposed framework (as well as its counterparts on the molecular side) will play an increasingly important role.

## V. CONCLUSIONS

In this work, a new method has been presented to simulate Brownian motion with hydrodynamic memory effects in a continuum framework on the basis of the generalized Langevin equation (GLE). The fact that the method relies solely on continuum-based simulation techniques, without having to resort to molecular dynamics to determine the hydrodynamic memory kernel required for GLE-based Brownian motion, means that it can be applied to systems with both short- and long-range hydrodynamic interactions. The method was shown to be capable of simulating Brownian motion for a wide range of particle-to-fluid density ratios, covering values characteristic of both liquid–solid and gas–solid systems.

Furthermore, the method was also shown to be able to simulate Brownian motion adjacent to a wall, thereby demonstrating its ability to incorporate effects on Brownian motion due to the presence of geometric variations in the particle neighborhood. These domain changes were also conveyed into the particle dynamics via the hydrodynamic memory kernel. The ability of the memory kernel to carry the relevant temporal and spatial hydrodynamic information allows for this simulation technique to be extended to more complicated geometries. The simulations can also be extended to include multiple particles as well as various background fluids, allowing for accurate modeling of multiphase phenomena at the micro- and nano-scales.

The hydrodynamic memory kernel, which is obtained on-the-fly as an intrinsic feature of the developed methodology, inherently reflects changes in the spatiotemporal behavior of the Brownian particle that come about due to added mass and history effects in the particle surroundings, which are especially relevant at low particle-to-fluid density ratios. It has been outlined how analyses of the kernel itself may be leveraged to obtain detailed information about the hydrodynamic environment surrounding individual particles. This spatiotemporal characterization of the particle environment may be further correlated with particle reactivity in non-inert systems, implying that the method represents a means of providing highly resolved information on how observations of particle motion may produce insight into evolving particle properties and be used to extend the functionality of surface-based sensing techniques.

## ACKNOWLEDGMENTS

This work has been financed by the Swedish Research Council (Vetenskapsrådet) via grant agreement Dnr 2021-05175. The computations were enabled by resources provided by the National

Academic Infrastructure for Supercomputing in Sweden (NAISS), partially funded by the Swedish Research Council (Vetenskapsrådet) through Grant Agreement No. 2022-06725.

## AUTHOR DECLARATIONS

### Conflict of Interest

The authors have no conflicts to disclose.

### Author Contributions

**Anand Joseph Michael:** Conceptualization (equal); Formal analysis (lead); Methodology (lead); Resources (supporting); Software (lead); Validation (lead); Visualization (lead); Writing – original draft (lead). **Andreas Mark:** Conceptualization (equal); Methodology (equal); Software (equal); Supervision (equal); Writing – review & editing (equal). **Srdjan Sasic:** Conceptualization (equal); Methodology (equal); Supervision (equal); Writing – review & editing (equal). **Henrik Ström:** Conceptualization (equal); Funding acquisition (lead); Methodology (equal); Project administration (lead); Resources (lead); Software (equal); Supervision (equal); Writing – review & editing (equal).

### DATA AVAILABILITY

The data that support the findings of this study are available from the corresponding author upon reasonable request.

### REFERENCES

- <sup>1</sup>T. M. Squires and S. R. Quake, “Microfluidics: Fluid physics at the nanoliter scale,” *Rev. Mod. Phys.* **77**, 977–1026 (2005).
- <sup>2</sup>E. Reimhult and F. Höök, “Design of surface modifications for nanoscale sensor applications,” *Sensors* **15**, 1635–1675 (2015).
- <sup>3</sup>L. Volpatti and A. Yetisen, “Commercialization of microfluidic devices,” *Trends Biotechnol.* **32**, 347–350 (2014).
- <sup>4</sup>X. Bian, C. Kim, and G. E. Karniadakis, “111 years of Brownian motion,” *Soft Matter* **12**, 6331–6346 (2016).
- <sup>5</sup>T. M. Squires and T. G. Mason, “Fluid mechanics of microrheology,” *Annu. Rev. Fluid Mech.* **42**, 413–438 (2010).
- <sup>6</sup>E. Frey and K. Kroy, “Brownian motion: A paradigm of soft matter and biological physics,” *Ann. Phys.* **517**, 20–50 (2005).
- <sup>7</sup>P. Hänggi and F. Marchesoni, “Artificial Brownian motors: Controlling transport on the nanoscale,” *Rev. Mod. Phys.* **81**, 387–442 (2009).
- <sup>8</sup>T. Franosch, M. Grimm, M. Belushkin, F. M. Mor, G. Foffi, L. Forró, and S. Jeney, “Resonances arising from hydrodynamic memory in Brownian motion,” *Nature* **478**, 85–88 (2011).
- <sup>9</sup>D. Pérez-Guerrero, B. Morales-Cruzado, G. Guerrero-García, and E. Sarmiento-Gómez, “On the Brownian motion of a colloid trapped in optical tweezers: Experiments and simulations,” *Am. J. Phys.* **92**, 290–298 (2024).
- <sup>10</sup>D. Gordon, V. Krishnamurthy, and S.-H. Chung, “Generalized Langevin models of molecular dynamics simulations with applications to ion channels,” *J. Chem. Phys.* **131**, 134102 (2009).
- <sup>11</sup>M. Lavaud, T. Salez, Y. Louyer, and Y. Amarouchene, “Stochastic inference of surface-induced effects using Brownian motion,” *Phys. Rev. Res.* **3**, L032011 (2021).
- <sup>12</sup>B. J. Alder and T. Wainwright, “Decay of the velocity autocorrelation function,” *Phys. Rev. A* **1**, 18 (1970).
- <sup>13</sup>J. C. Chen and A. S. Kim, “Brownian dynamics, molecular dynamics, and Monte Carlo modeling of colloidal systems,” *Adv. Colloid Interface Sci.* **112**, 159–173 (2004).
- <sup>14</sup>H. K. Shin, C. Kim, P. Talkner, and E. K. Lee, “Brownian motion from molecular dynamics,” *Chem. Phys.* **375**, 316–326 (2010).
- <sup>15</sup>A. S. Kannan, V. Naserentin, A. Mark, D. Maggiolo, G. Sardina, S. Sasic, and H. Ström, “A continuum-based multiphase DNS method for studying the Brownian dynamics of soot particles in a rarefied gas,” *Chem. Eng. Sci.* **210**, 115229 (2019).
- <sup>16</sup>P. Langevin *et al.*, “Sur la théorie du mouvement brownien,” *C. R. Acad. Sci. Paris* **146**, 530 (1908).
- <sup>17</sup>R. Kubo, “The fluctuation-dissipation theorem,” *Rep. Prog. Phys.* **29**, 255 (1966).
- <sup>18</sup>J. F. Brady and G. Bossis *et al.*, “Stokesian dynamics,” *Annu. Rev. Fluid Mech.* **20**, 111–157 (1988).
- <sup>19</sup>H. Ounis, G. Ahmadi, and J. B. McLaughlin, “Brownian diffusion of submicrometer particles in the viscous sublayer,” *J. Colloid Interface Sci.* **143**, 266–277 (1991).
- <sup>20</sup>A. Li and G. Ahmadi, “Dispersion and deposition of spherical particles from point sources in a turbulent channel flow,” *Aerosol Sci. Technol.* **16**, 209–226 (1992).
- <sup>21</sup>T. Iwashita, Y. Nakayama, and R. Yamamoto, “A numerical model for Brownian particles fluctuating in incompressible fluids,” *J. Phys. Soc. Jpn.* **77**, 074007 (2008).
- <sup>22</sup>F. Mainardi, A. Mura, and F. Tampieri, “Brownian motion and anomalous diffusion revisited via a fractional Langevin equation,” [arXiv:1004.3505](https://arxiv.org/abs/1004.3505) (2010).
- <sup>23</sup>A. B. Basset, *A Treatise on Hydrodynamics: With Numerous Examples* (Deighton, Bell, and Company, 1888), Vol. 2.
- <sup>24</sup>J. W. Dufty, “Gaussian model for fluctuation of a Brownian particle,” *Phys. Fluids* **17**, 328–333 (1974).
- <sup>25</sup>E. Hauge and A. Martin-Löf, “Fluctuating hydrodynamics and Brownian motion,” *J. Stat. Phys.* **7**, 259–281 (1973).
- <sup>26</sup>G. Jung, M. Hanke, and F. Schmid, “Generalized Langevin dynamics: Construction and numerical integration of non-Markovian particle-based models,” *Soft Matter* **14**, 9368–9382 (2018).
- <sup>27</sup>G. Jung and F. Schmid, “Frequency-dependent hydrodynamic interaction between two solid spheres,” *Phys. Fluids* **29**, 126101 (2017).
- <sup>28</sup>A. Obliger, “Simple and efficient algorithms based on Volterra equations to compute memory kernels and projected cross-correlation functions from molecular dynamics,” *J. Chem. Phys.* **158**, 144101 (2023).
- <sup>29</sup>M. Kerr Winter, I. Pihlajamaa, V. E. Debets, and L. Janssen, “A deep learning approach to the measurement of long-lived memory kernels from generalized Langevin dynamics,” *J. Chem. Phys.* **158**, 244115 (2023).
- <sup>30</sup>P. Xie, R. Car, and E. Weinan, “Ab initio generalized Langevin equation,” *Proc. Natl. Acad. Sci. U. S. A.* **121**, e2308668121 (2024).
- <sup>31</sup>A. J. Ladd, “Short-time motion of colloidal particles: Numerical simulation via a fluctuating lattice-Boltzmann equation,” *Phys. Rev. Lett.* **70**, 1339 (1993).
- <sup>32</sup>P. J. Atzberger, “Velocity correlations of a thermally fluctuating Brownian particle: A novel model of the hydrodynamic coupling,” *Phys. Lett. A* **351**, 225–230 (2006).
- <sup>33</sup>Y. Nakayama, Y. Matsuoka, and T. Kajiwara, “Simulating Brownian motion in thermally fluctuating viscoelastic fluids by using the smoothed profile method,” *J. Comput. Phys.* **509**, 113035 (2024).
- <sup>34</sup>G. De Fabritiis, M. Serrano, R. Delgado-Buscalioni, and P. Coveney, “Fluctuating hydrodynamic modeling of fluids at the nanoscale,” *Phys. Rev. E* **75**, 026307 (2007).
- <sup>35</sup>J. Vom Scheidt, P. Kloeden, and E. Platen, “Numerical solution of stochastic differential equations,” *ZAMM J. Appl. Math. Mech.* **74**, 332 (1994).
- <sup>36</sup>A. Donev, A. Nonaka, A. Bhattacharjee, A. Garcia, and J. Bell, “Low Mach number fluctuating hydrodynamics of multispecies liquid mixtures,” *Phys. Fluids* **27**, 037103 (2015).
- <sup>37</sup>G. G. Stokes *et al.*, *On the Effect of the Internal Friction of Fluids on the Motion of Pendulums* (Cambridge University Press, 1851).
- <sup>38</sup>D. Chakraborty, “Velocity autocorrelation function of a Brownian particle,” *Eur. Phys. J. B* **83**, 375 (2011).
- <sup>39</sup>E. Lauga and T. Squires, “Brownian motion near a partial-slip boundary: A local probe of the no-slip condition,” *Phys. Fluids* **17**, 103012 (2005).
- <sup>40</sup>A. Simha, J. Mo, and P. Morrison, “Unsteady Stokes flow near boundaries: The point-particle approximation and the method of reflections,” *J. Fluid Mech.* **841**, 883–924 (2018).
- <sup>41</sup>M. Maxey and J. Riley, “Equation of motion for a small rigid sphere in a non-uniform flow,” *Phys. Fluids* **26**, 883–889 (1983).

- <sup>42</sup>A. Mark and B. G. van Wachem, "Derivation and validation of a novel implicit second-order accurate immersed boundary method," *J. Comput. Phys.* **227**, 6660–6680 (2008).
- <sup>43</sup>D. Liu and J. Nocedal, "On the limited memory method for large scale optimization," *Math. Program. B* **45**, 503–528 (1989).
- <sup>44</sup>R. Byrd, P. Lu, J. Nocedal, and C. Zhu, "A limited memory algorithm for bound constrained optimization," *SIAM J. Sci. Comput.* **16**, 1190–1208 (1995).
- <sup>45</sup>C. Zhu, R. Byrd, P. Lu, and J. Nocedal, "L-BFGS-B: Algorithm 778: L-BFGS-B, Fortran routines for large scale bound constrained optimization," *ACM Trans. Math. Software* **23**, 550–560 (1997).
- <sup>46</sup>P. Virtanen, R. Gommers, T. E. Oliphant, M. Haberland, T. Reddy, D. Cournapeau, E. Burovski, P. Peterson, W. Weckesser, J. Bright, S. J. van der Walt, M. Brett, J. Wilson, K. J. Millman, N. Mayorov, A. R. J. Nelson, E. Jones, R. Kern, E. Larson, C. J. Carey, Í. Polat, Y. Feng, E. W. Moore, J. VanderPlas, D. Laxalde, J. Perktold, R. Cimrman, I. Henriksen, E. A. Quintero, C. R. Harris, A. M. Archibald, A. H. Ribeiro, F. Pedregosa, P. van Mulbregt, and SciPy 1.0 Contributors, "SciPy 1.0: Fundamental algorithms for scientific computing in Python," *Nat. Methods* **17**, 261–272 (2020).
- <sup>47</sup>A. R. Conn, N. I. Gould, and P. L. Toint, *Trust Region Methods* (SIAM, 2000).
- <sup>48</sup>N. Newmark, "A method of computation for structural dynamics," *J. Eng. Mech. Div.* **85**, 67–94 (1959).
- <sup>49</sup>K. Itô, "Stochastic integration," in *Vector and Operator Valued Measures and Applications* (Elsevier, 1973), pp. 141–148.
- <sup>50</sup>A. Mark, R. Rundqvist, and F. Edelvik, "Comparison between different immersed boundary conditions for simulation of complex fluid flows," *Fluid Dyn. Mater. Process.* **7**, 241–258 (2011).
- <sup>51</sup>A. Einstein, "Über die von der molekularkinetischen Theorie der Wärme geforderte Bewegung von in ruhenden Flüssigkeiten suspendierten Teilchen," *Ann. Phys.* **322**, 549–560 (1905).
- <sup>52</sup>P. Alexander, "High order computation of the history term in the equation of motion for a spherical particle in a fluid," *J. Sci. Comput.* **21**, 129–143 (2004).
- <sup>53</sup>L. Wakaba and S. Balachandar, "History force on a sphere in a weak linear shear flow," *Int. J. Multiphase Flow* **31**, 996–1014 (2005).
- <sup>54</sup>B. Felderhof, "Effect of the wall on the velocity autocorrelation function and long-time tail of Brownian motion," *J. Phys. Chem. B* **109**, 21406–21412 (2005).
- <sup>55</sup>S. Jeney, B. Lukic, J. Kraus, T. Franosch, and L. Forró, "Anisotropic memory effects in confined colloidal diffusion," *Phys. Rev. Lett.* **100**, 240604 (2008).
- <sup>56</sup>I. Pagonabarraga, M. Hagen, C. Lowe, and D. Frenkel, "Algebraic decay of velocity fluctuations near a wall," *Phys. Rev. E* **58**, 7288–7295 (1998).
- <sup>57</sup>K. Huang and I. Szlufarska, "Effect of interfaces on the nearby Brownian motion," *Nat. Commun.* **6**, 8558 (2015).
- <sup>58</sup>A. Banerjee and K. Kihm, "Experimental verification of near-wall hindered diffusion for the Brownian motion of nanoparticles using evanescent wave microscopy," *Phys. Rev. E* **72**, 042101 (2005).
- <sup>59</sup>K. Berg-Sorensen and H. Flyvbjerg, "The colour of thermal noise in classical Brownian motion: A feasibility study of direct experimental observation," *New J. Phys.* **7**, 38 (2005).
- <sup>60</sup>A. Jannasch, M. Mahamdeh, and E. Schäffer, "Inertial effects of a small Brownian particle cause a colored power spectral density of thermal noise," *Phys. Rev. Lett.* **107**, 228301 (2011).
- <sup>61</sup>A. Goldman, R. Cox, and H. Brenner, "Slow viscous motion of a sphere parallel to a plane wall—I Motion through a quiescent fluid," *Chem. Eng. Sci.* **22**, 637–651 (1967).
- <sup>62</sup>M. Bevan and D. Prieve, "Hindered diffusion of colloidal particles very near to a wall: Revisited," *J. Chem. Phys.* **113**, 1228–1236 (2000).
- <sup>63</sup>G. E. Uhlenbeck and L. S. Ornstein, "On the theory of the Brownian motion," *Phys. Rev.* **36**, 823 (1930).
- <sup>64</sup>S. Chandrasekhar, "Stochastic problems in physics and astronomy," *Rev. Mod. Phys.* **15**(1), 1 (1943).
- <sup>65</sup>A. S. Kannan, A. Mark, D. Maggiolo, G. Sardina, S. Sasic, and H. Ström, "A hydrodynamic basis for off-axis Brownian diffusion under intermediate confinements in micro-channels," *Int. J. Multiphase Flow* **143**, 103772 (2021).
- <sup>66</sup>Z. Li, X. Bian, X. Li, and G. E. Karniadakis, "Incorporation of memory effects in coarse-grained modeling via the Mori-Zwanzig formalism," *J. Chem. Phys.* **143**, 243128 (2015).
- <sup>67</sup>G. Jung, M. Hanke, and F. Schmid, "Iterative reconstruction of memory kernels," *J. Chem. Theory Comput.* **13**, 2481–2488 (2017).
- <sup>68</sup>H. Ström, J. Sjöblom, A. Kannan, H. Ojagh, O. Sundborg, and J. Koeqler, "Near-wall dispersion, deposition and transformation of particles in automotive exhaust gas aftertreatment systems," *Int. J. Heat Fluid Flow* **70**, 171–180 (2018).
- <sup>69</sup>J. Sjöblom and H. Ström, "Capture of automotive particulate matter in open substrates," *Ind. Eng. Chem. Res.* **52**, 8373–8385 (2013).
- <sup>70</sup>M. Connaughton and M. Dabagh, "Modeling physical forces experienced by cancer and stromal cells within different organ-specific tumor tissue," *IEEE J. Transl. Eng. Health Med.* **12**, 413–434 (2024).
- <sup>71</sup>E. Kätelhön, S. Sokolov, and R. Compton, "Near-wall hindered diffusion: Implications for surface-based sensors," *Sens. Actuators, B* **234**, 420–425 (2016).
- <sup>72</sup>W. Fei, Y. Gu, and K. Bishop, "Active colloidal particles at fluid-fluid interfaces," *Curr. Opin. Colloid Interface Sci.* **32**, 57–68 (2017).
- <sup>73</sup>J. Anderson, "Colloid transport by interfacial forces," *Annu. Rev. Fluid Mech.* **21**, 61–99 (1989).
- <sup>74</sup>F. Möller, F. Kriegel, M. Kieß, V. Sojo, and D. Braun, "Steep pH gradients and directed colloid transport in a microfluidic alkaline hydrothermal pore," *Angew. Chem. Int. Ed.* **56**, 2340–2344 (2017).
- <sup>75</sup>S. Shin, "Diffusiophoretic separation of colloids in microfluidic flows," *Phys. Fluids* **32**, 101302 (2020).
- <sup>76</sup>C. Hohenegger and S. A. McKinley, "Fluid–particle dynamics for passive tracers advected by a thermally fluctuating viscoelastic medium," *J. Comput. Phys.* **340**, 688–711 (2017).
- <sup>77</sup>S. Ingelsten, A. Mark, and F. Edelvik, "A Lagrangian-Eulerian framework for simulation of transient viscoelastic fluid flow," *J. Non-Newtonian Fluid Mech.* **266**, 20–32 (2019).